Auto-regulatory J-domain interactions control Hsp70 recruitment in the oligomeric DNAJB8 co-chaperone

Bryan D. Ryder[1,2], Irina Matlahov[3], Sofia Bali[1,2], Jaime Vaquer-Alicea[2,4], Patrick C.A. van der Wel[3,5,*], Lukasz A. Joachimiak[2,6,*]

[1] Molecular Biophysics Graduate Program, University of Texas Southwestern Medical Center, Dallas, TX 75390, United States

[2] Center for Alzheimer's and Neurodegenerative Diseases, University of Texas Southwestern Medical Center, Dallas, TX 75390, United States

[3] Department of Structural Biology, University of Pittsburgh School of Medicine, Pittsburgh, PA 15213, USA

[4] Neuroscience Graduate Program, University of Texas Southwestern Medical Center, Dallas, TX 75390, United States

[5] Zernike Institute for Advanced Materials, University of Groningen, 9747 AG Groningen, Netherlands

[6] Department of Biochemistry, University of Texas Southwestern Medical Center, Dallas, TX 75390, United States

[*] Correspondence: Lukasz.Joachimiak@utsouthwestern.edu, p.c.a.van.der.wel@rug.nl

Abstract

The Hsp40/Hsp70 chaperone families combine a versatile folding capacity with high specificity, which is mainly facilitated by Hsp40s. The structure and function of many Hsp40s remain poorly understood, with the oligomeric Hsp40s particularly refractory to characterization. Yet, structural insight on the architecture and dynamics of these oligomeric Hsp40s will help explain their potent ability to suppress polyglutamine and other amyloid protein aggregation. Here, our combined *in vitro*, *in vivo,* and *in silico* studies shed new light on the supramolecular structure of the homooligomeric Hsp40 DnaJB8 and how it regulates recruitment of partner Hsp70s. We identify in the oligomers an interaction between the J-Domain (JD) and the beta-sheet-rich C-terminal domain (CTD), causing the sequestration of the JD, and occlusion of its surface necessary for Hsp70 recruitment. We propose a new model for DnaJB8 activity in which a built-in autoinhibitory switch reversibly controls the recruitment of Hsp70. These results provide evidence that the evolutionarily conserved CTD of DnaJB8, and related Hsp40s, serves as an essential regulatory element of their pivotal role in cellular proteostasis.

INTRODUCTION

Molecular chaperones play central roles in cellular homeostasis by facilitating protein folding, directing protein folding quality control, and refolding stress-denatured substrates. Structural descriptions of chaperone architecture and conformational cycles have been key to understanding their biological function. Thus, functional insight into chaperones relies on structural biology tools such as NMR, cryo-EM and X-ray crystallography[1-7]. This structural information has been used to identify substrate binding sites, key conformational changes that drive substrate release, and the role of ATP hydrolysis. A molecular view of chaperones is essential to explain chaperones' biological function in protein folding and suggest new avenues for treating protein misfolding diseases.

The cellular chaperone network needs to handle a wide variety of protein substrates in numerous different (mis)folded states. This demands a combination of broad versatility and specificity in terms of substrate recognition, even though the central players Hsp70 and Hsp90 are highly conserved. This apparent contradiction is resolved by the Hsp40 (DnaJ) family of proteins, which are co-chaperones that recruit and regulate the activity of Hsp70 chaperones in refolding misfolded proteins[8-11]. While the human Hsp70 family is highly conserved, the Hsp40 co-chaperone family encodes 47 diverse members, each with specialized functions in substrate recognition and presumed coordination with Hsp70[12-14]. DnaJ proteins feature a J-domain (JD), which binds to Hsp70s through a conserved electrostatic interaction to trigger ATP hydrolysis by the Hsp70[1, 14-16]. This in turn initiates a conformational rearrangement in the substrate binding domain of the Hsp70 that helps capture an unfolded substrate for folding, refolding, or disaggregation[17]. In cases when misfolded proteins cannot be refolded, some Hsp40s help direct proteins for degradation[18-19]. However, the mechanistic details of how different Hsp40s recruit Hsp70 or their substrates remain unknown. Furthermore, while it is known that the Hsp70 can interact with JDs through electrostatic surfaces it remains unclear how JD binding to Hsp70 is controlled to specific and/or activated Hsp40 proteins.

In humans, Hsp40s are classified into A, B, and C sub-families, in which members typically function as monomers, dimers, or polydisperse oligomers. For example, the A family Hsp40s (DnaJA1-A4) and a subset of B family Hsp40s (DnaJB1/B4/B5), all encode a globular domain architecture similar to the bacterial Hsp40 DnaJ. These classical Hsp40 members assemble into homo-dimers through conserved C-terminal motifs and bind unfolded substrates through conserved β-barrel C-terminal domains (CTD)[20]. Recent evidence suggests that this subset of Hsp40s can form mixed hetero-dimers driven by electrostatic contacts to expand the substrate recognition repertoire[21].

A different set of non-classical Hsp40 B family members (DnaJB2, DnaJB6b, DnaJB7 and DnaJB8) encode a domain architecture that is distinct from the classical dimeric DnaJ orthologs. Rather than encoding a classical β-barrel CTD, their C-terminus encodes a different architecture [22-23]. Of these 4 members, the DnaJB8 and DnaJB6b proteins have been shown to assemble into oligomers *in vitro* and *in vivo*[22, 24-25]. The role of the CTD in these chaperones remains unclear, and the literature reveals conflicting results, suggesting either that it drives oligomerization or that it mediates intramolecular contacts[22-24, 26]. The functional role of the oligomeric state of DnaJB6b and DnaJB8 remains unclear, although it has been proposed to serve as a type of phase-separated storage form capable of capturing substrates[25]. The characteristic structural and dynamic heterogeneity of the oligomers has greatly hindered efforts to study them, with recent structural studies resorting to deletion mutants to gain structural insight[22-23]. A combination of variables, including large size and polydispersity, has made these chaperones recalcitrant to both classical and modern structural biology methods, including cryoEM[25].

The oligomeric chaperones DnaJB6b and DnaJB8 have been shown to be potent suppressors of aggregation of amyloid proteins in cells and *in vitro* [22, 26]. Despite several studies demonstrating a role for DnaJB6b in suppressing assembly of amyloid-prone substrates it is unclear exactly how it interacts with substrates, and how oligomerization

118 plays a role in this process. The serine/threonine domain of DnaJB6b is important for
119 suppression of mutant huntingtin protein aggregation in cells,[27] and its deletion limits
120 oligomerization yielding a stable monomer at the expense of activity[23]. In absence of a
121 comprehensive understanding of the full-length structural behavior for this class of DnaJ
122 chaperones, it remains unclear how they fulfill their critical function to protect the
123 proteome from aggregation.
124
125 Here we examine in unprecedented detail the DnaJB8 variant. DnaJB8 was shown to be
126 particularly effective at preventing formation of polyglutamine deposits, even more so than
127 DnaJB6b, despite 63 % sequence identity[22, 27]. Notably, unlike other chaperones that
128 inhibit mutant huntingtin aggregation[28], DnaJB8 and DnaJB6b are thought to target and
129 bind the expanded polyglutamine domain itself and thus are active across the whole
130 family of polyglutamine diseases[22, 27]. The assembly of DnaJB8 into dynamic and
131 heterogeneous high molecular weight complexes (polydisperse oligomers) has thus far
132 prevented their detailed characterization by traditional structural biology approaches. To
133 address this challenge, we applied a hybrid structural biology approach to understand the
134 architecture and dynamics of the DnaJB8 oligomer. We observe that DnaJB8 assembles
135 into large oligomers *in vitro* and *in vivo*. We used crosslinking mass spectrometry (XL-
136 MS) to identify local intra-domain contacts and long-range contacts mediated by
137 complementary electrostatic surfaces. We show that changes in ionic strength modulate
138 the assembly and topology of oligomer, which points to the important role of charge-
139 charge interactions. Using multidimensional solid-state NMR (ssNMR) we probe the
140 structural and dynamic disorder of the solvated oligomers. Dramatic domain-specific
141 differences in line widths, resolution, and peak intensity indicate that the oligomers feature
142 a range of (dis)order, but lack highly flexible regions. The JD transitions between a
143 strikingly ordered immobilized state and a more mobilized state in response to
144 electrostatic disruption. We show that the JD and CTD terminal domains are monomeric
145 in isolation, but form heterodimers when mixed, reconstituting interactions observed in
146 oligomers. Finally, we demonstrate that the DnaJB8 JD-CTD contacts regulate the

147 recruitment of Hsp70. Thus, we identify and validate the first example of a DnaJ protein
148 encoding a built-in regulatory domain that controls its recruitment (and activation) of
149 Hsp70.
150

151 RESULTS

152 **DnaJB8 JD binds to HspA1A using a conserved electrostatic surface**

153 Recent crystallographic analysis of the bacterial DnaK:DnaJ complex revealed the
154 binding mode of the complex[16], which validated previous insight from NMR and
155 biochemical data[15]. The model proposed an electrostatically driven interaction between
156 the basic surfaces on helices 2 and 3 on the DnaJ and an acidic surface on the DnaK that
157 spans the Nucleotide Binding Domain (NBD) and the Substrate Binding Domain (SBD)[16].
158 The JD includes a conserved Histidine-Proline-Aspartic acid (HPD) motif between helices
159 2 and 3 that recruits Hsp70 and stimulates ATP hydrolysis for substrate capture[29]. Using
160 the DnaK model (PDB id: 5NRO) as a template we employed Rosetta to build a homology
161 model of the human HspA1A homolog[16]. The HspA1A model shows good structural
162 agreement with the DnaK homolog (Figure 1A) and also presents a conserved acidic
163 surface that spans the NBD and SBD (Supplementary Figure 1A-C). Using the
164 DnaK:DnaJ complex structure, we modeled the binding interface between the HspA1A
165 homology model and the experimentally determined structure of the JD of DnaJB8[30]
166 (Figure 1B-C). The basic surface on the DnaJB8 JD (Figure 1B) contacts the conserved
167 acidic surface on the HspA1A (Figure 1C, S1D-E). Thus, conserved electrostatic contacts
168 are likely to play a key role in the interaction between Hsp70 and Hsp40.
169

170 The DnaJB8 co-chaperone is predicted to encode three domains C-terminal to the
171 N-terminal JD (Figure 1D): a phenylalanine and glycine (F/G) rich domain (Figure 1D,
172 blue), a serine/threonine rich (S/T) domain (Figure 1D, cyan) and a C-terminal CTD
173 (Figure 1D, green). Secondary structure analysis on the DnaJB8 sequence reveals the
174 N-terminal JD fold but also predicts the CTD to adopt a five-stranded β-pleated sheet,
175 consistent with the conformation observed in the homologous DnaJB6b[31-32](Figure 1E).

176 The basic surface on JD helix 2 in DnaJB8 mediates binding to Hsp70, but we see that
177 there is surface charge complementarity to the CTD, which is similar to the same
178 complementarity expected from the JD-Hsp70 interaction (Figure 1F). The middle F/G
179 and S/T domains are unstructured (Figure 1G) and contain sequences with lower
180 complexity, particularly in the S/T domain. In studies of DnaK/DnaJ, it was seen that the
181 DnaK F/G domain does not bind directly to its Hsp70 counterpart, but it is involved in
182 regulation of the substrate binding activity of DnaK[10]. In patients, mutations in the F/G
183 domain of the homologous DnaJB6b (Supplementary Figure 1F) (including F89I, F93L,
184 P96R and F100V) cause autosomal limb-girdle muscular dystrophy diseases that exhibit
185 similar, but not identical clinical outcomes. Recent studies have shown that the JD-
186 proximal region of the F/G domain in DnaJB6b can adopt a short helix that weakly
187 interacts with the JD [23], which may be relevant to the disease-causing mutations since
188 they are found within this helix[24, 27]. The low complexity S/T domain has been proposed
189 to play a key role in the activity of DnaJB6b to inhibit polyglutamine aggregation[27].
190 Altogether, it is clear that charge complementarity is important for the Hsp70:Hsp40
191 interaction, but that there is also a role for DnaJB8 interactions and domains beyond the
192 JD.
193
194 **Interactions of oligomeric DnaJB8 in a cellular context**
195 Prior studies have highlighted the ability of DnaJB8 to assemble into oligomers but have
196 failed to provide insights into the interactions that drive oligomer formation [22, 26]. We first
197 asked whether DnaJB8 can form oligomers in cells by expressing DnaJB8 fused to a
198 green fluorescent protein (GFP) derivative: Clover (herein, DnaJB8-Cover) in HEK293
199 cells (Figure 2A). We observed the formation of fluorescent juxtanuclear puncta that
200 localize close to the nucleus (Figure 2B). Puncta were not observed in control cells
201 expressing Clover alone (Figure 2B). When quantified, 39.2±3.1% of the cells expressing
202 DnaJB8-Clover contain puncta while only 0.44±0.50% of the control cells contained
203 puncta (Figure 2C). To test the concentration dependence on puncta formation, we
204 assayed the frequency of puncta with different levels of expression and observed 4-fold

205 lower protein levels reduced the DnaJB8-Clover puncta frequency to 17.5±10.3% (Figure
206 2C). The puncta frequency for Clover alone remained below 1% in the two experiments
207 (Figure 2C). From microscopy images we estimate the DnaJB8-Clover puncta to have a
208 maximum diameter of 1.0µm (Figure 2B).
209
210 We next sought to characterize biochemical properties of DnaJB8-Clover expressed in
211 mammalian cells. To isolate the Clover protein, we used α-GFP nano-bodies[33-34] allowing
212 immunoprecipitation (IP) of the DnaJB8-Clover fusion and Clover from HEK293 cells.
213 Western blot analysis of the purified IP fractions confirms the presence of DnaJB8 and
214 Clover using α-GFP and α-DnaJB8 antibodies (Supplementary Figure 2A) in the DnaJB8-
215 Clover and control cell lines. The IP purified samples were first analyzed by a proteomic
216 mass spectrometry approach to identify any candidate proteins associated with DnaJB8-
217 Clover. Using the CPFP[35] software we identified 60 proteins that were enriched in the
218 DnaJB8-Clover samples relative to the control Clover sample (Supplementary Figure 2B
219 and Supplementary Data 1). Among the enriched proteins we found other chaperones
220 including the eukaryotic chaperonin TRiC/CCT, Hsp90A/B, HspD1, and two Hsp70 family
221 members: HspA8 and HspA1A (Supplementary Figure 2C). *A priori*, one might expect to
222 see an enrichment in Hsp70, but the levels of Hsp70 enrichment in the IP were minor
223 relative to the Clover controls, suggesting that the DnaJB8:Hsp70 interaction is weak
224 under the conditions used, despite the known Hsp40:Hsp70 relationship.
225
226 Combining crosslinking with mass spectrometry can help define contact points in
227 proteins and protein complexes, with particular importance for systems not tractable for
228 classical structural biology methods[36-38]. After isolation of DnaJB8-Clover using an α-GFP
229 nanobody IP, we reacted the samples with a combination of adipic acid dihydrazide (ADH)
230 and 4-(4,6-dimethoxy-1,3,5-triazin-2-yl)-4-methyl-morpholinium chloride (DMTMM),
231 respectively. ADH covalently links carboxylate-carboxylate contacts via a 6-carbon
232 bridge, while DMTMM acts as a chemical intermediate to form a direct covalent bond
233 between lysine-carboxylate groups through dehydration[37]. The latter reaction is referred
234 to as a "zero-length" crosslink since no additional atoms are added in order to link the two

235 target groups. Crosslinking treatment yielded a high molecular weight species, consistent
236 with an oligomeric form (Figure 2D). To identify whether inter-domain contacts were
237 present in these oligomers, we employed XL-MS on the DnaJB8-Clover purified by IP
238 from mammalian cells. We identified 1 carboxylate-carboxylate and 20 lysine-carboxylate
239 crosslinks that parsed into three coarse regions: JD-JD, CTD-CTD and JD-CTD (Figure
240 2C, Supplementary Data 2). The three local JD contacts (Figure 2C; JD contacts in red
241 box) linking K25-D37, K34-D37 and E41-K34 are consistent with the known structural
242 model of the domain (Supplementary Figure 2D). Local CTD contacts were also
243 accompanied by inter-domain JD-CTD contacts that localize to helices 2 and 3 (Figure
244 2C, JD-CTD contacts in grey box). Additionally, we identified a contact between K34 in
245 the JD and D97 that is consistent with a weak interaction between the JD and a putative
246 helix 5 of the F/G domain identified in the homologous DnaJB6b[23]. DnaJB8-Clover
247 oligomers isolated from mammalian cells reveal an array of inter-domain interactions,
248 including contacts between the charge complementary JD and CTD.
249

250 **DnaJB8 JD-CTD contacts are preserved *in vitro***

251 To enable a more detailed understanding of DnaJB8 oligomerization, we sought to
252 reconstitute DnaJB8 oligomers *in vitro*. Full length DnaJB8 was produced recombinantly
253 and purified as previously described[22]. We used Dynamic Light Scattering (DLS) and
254 Transmission Electron Microscopy (TEM) to detect DnaJB8 oligomers forming in solution
255 over time. We initially observe DnaJB8 species with an average radius of hydration (R_h)
256 of 13.7±2.5nm which after 8 hours steadily increase in size, eventually reaching a
257 maximum average R_h of 91.9±12.6nm after 15 hours (Figure 3A, Supplementary Data 3).
258 While the average R_h is informative for interpretation of the kinetics of assembly, the
259 derived values do not reflect real species. Partitioning the scattering data into bins with
260 different radii reveals *bona fide* sizes: DnaJB8 primarily begins as a small species
261 (5.54±2.36nm) with a small (<%1 by mass) contribution of larger species (>100nm) but
262 as aggregation progresses the small species are converted into larger assemblies (30.6%
263 by mass) (Supplementary Figure 3A). We next used negative-stain TEM to visualize the

264 DnaJB8 oligomers at 15 hours where we first observed the formation of larger species by
265 DLS. Upon imaging the grids, we found elongated polydisperse oligomeric structures with
266 varying lengths around 90nm, and widths of approximately 20nm along with amorphous
267 oligomeric species (Figure 3B). These findings are consistent with prior studies on
268 DnaJB6b and DnaJB8 showing that it can form oligomers *in vitro*[22, 24-25, 27, 39].
269 Next, we aimed to better understand the topology of these *in vitro* oligomers by XL-MS,
270 using two parallel chemistries; disuccinimidyl suberate (DSS) and ADH/DMTMM (Figure
271 2D). Consistent with the formation of oligomers, we observe by SDS-PAGE a ladder of
272 bands indicating the covalent trapping of intermolecular contacts (Supplementary Figure
273 3B). Notably, the ADH/DMTMM chemistry yielded a higher efficiency of trapping
274 oligomeric species than DSS, which has been previously used to probe structure of the
275 related DnaJB6b[25]. XL-MS analysis of these samples showed only three crosslinks in the
276 DSS condition (Figure 3C, Supplementary Data 2). In contrast, the ADH/DMTMM analysis
277 yielded 18 lysine-carboxylate crosslinks and 6 carboxylate-carboxylate crosslinks that
278 localize to three main regions (Figure 3C, Supplementary Data 2): within the JD (Figure
279 3C, red dashed box), within the CTD (Figure 3C, green dashed box), and contacts
280 between JD and CTD (Figure 3C, grey dashed box). This pattern closely matches those
281 observed in the assemblies recovered from the mammalian cells above. Within the JD,
282 there are five crosslinks; one carboxylate-carboxylate (D33-E43) and four lysine-
283 carboxylate crosslinks (K34-E40, K34-E41, D37-K45 and E54-K60) (Figure 3C). Out of
284 these five crosslinks, four of them are localized around the loop between helix 2 and helix
285 3, where the HPD motif responsible for Hsp70 binding is located. Mapping the crosslinks
286 onto the structure of the JD showed that the C_α-C_α distances varied across zero-length
287 crosslink pairs from 11.6Å to 14.7Å and the single ADH pair spanned 8.9Å
288 (Supplementary Figure 3C). These C_α-C_α distances are consistent for each chemistry,
289 with zero-length crosslink pair distances falling under 16Å and ADH-derived distances
290 spanning less than 20Å[37]. In addition, the side chains in each amino acid pair are solvent
291 accessible in the DnaJB8 JD structure (Supplementary Figure 3C). These data suggest
292 that the local JD crosslinks are consistent with intramolecular contacts within a JD
293 monomer.

294

295 The CTD region of DnaJB8 yielded two ADH-based crosslinks (E208-E224 and E210-
296 E224) and six lysine-carboxylate zero-length crosslinks (E211-K227, E208-K227, E210-
297 K227, E211-K223, K193-E211, and E211-K232) (Figure 3C). Amongst these, the local
298 regions spanning E208-E211 and K223-K227 are central to the CTD and repeatedly react
299 to peripheral sites. The third cluster of contacts linked the distal JD and CTD through four
300 lysine-carboxylate crosslinks (K34-D212, K47-E208, K47-E211, and K60-E211) (Figure
301 3C, inset). These long-range crosslinks span an average sequence separation of 163.5
302 amino acids separated by the central unstructured F/G and S/T domains. The CTD
303 crosslink sites are exclusively mediated through acidic amino acids; D212, E209 and
304 E211. Interestingly, the crosslinked amino acids on the JD are all lysines (K34, K47 and
305 K60) that localize to basic surfaces along each helix (Supplementary Figure 3D) and
306 overlap the basic Hsp70 binding surface[16]. Consistent with the *ex vivo* analysis we again
307 identified an isolated crosslink between the JD and the proposed helix 5 in the F/G
308 domain. Clearly, these XL-MS data point to an intricate network of inter-domain
309 interactions in the oligomeric DnaJB8.

310

311 To further test the apparent role of electrostatically driven inter-domain interactions, we
312 used a higher ionic strength buffer in an analogous series of experiments. Using DLS we
313 found the average R_h to remain stable at 13.7 ± 1.2 nm over time (Figure 3D,
314 Supplementary Data 3). A closer inspection of the scattering data reveals a predominance
315 of smaller species (7.75±0.7nm) alongside a small and unchanging contribution of larger
316 species (<1% by mass) (Supplementary Figure 3E). TEM showed that the latter species
317 are spherical with 10-20nm in diameter (Figure 3E). Thus, increased ionic strength inhibits
318 the formation of the more heterogenous larger (>100 nm) structures. DLS also shows that
319 the predominant species are more collapsed (5.54±2.36nm) in the low ionic strength
320 condition compared to that found in the higher salt (7.75±0.7nm) (Supplementary Figure
321 3F). XL-MS demonstrates that while some short-range crosslinks within either the JD or
322 the CTD are preserved, the long-range inter-domain contacts have now been lost (Figure

323 3F). To control for reactivity in each buffer condition we compared the frequency of ADH
324 driven monolinks. Monolinks occur when a chemical crosslinker reacts with a solvent
325 exposed residue on the target protein, but no other corresponding residues are in close
326 physical proximity to attack the other end of the crosslinker. These peptide fragments are
327 useful for identifying isolated surfaces, as well as validating the efficiency of the
328 crosslinker chemistry. The data show that the higher ionic strength has little effect on the
329 chemistry of DMTMM on acidic residues or the ability of ADH to target those same
330 residues (Supplementary Figure 3G). Thus, we observe the disruption of electrostatically
331 driven JD-CTD interactions being accompanied by changes in the domain architecture as
332 well as higher order assembly of DnaJB8 oligomers.
333
334 **ssNMR on DnaJB8 oligomers reveals regions of disorder and order**
335 To gain additional insight into their molecular structure and dynamics, multidimensional
336 magic-angle-spinning (MAS) ssNMR was performed on the hydrated oligomers of U-
337 ^{13}C,^{15}N-labeled DnaJB8. The MAS ssNMR signals of hydrated protein assemblies allow
338 for the site- and domain-specific detection of mobility and (secondary) structure, even in
339 presence of considerable disorder and heterogeneity. In 2D ssNMR spectra we observe
340 many broad peaks, with linewidths up to 0.38 kHz, consistent with an oligomeric assembly
341 displaying structural disorder (Figure 4A). However, strikingly, distinct subsets of narrow
342 peaks are also detected, with 1D projections showing linewidths of 0.1 to 0.2 kHz (Figure
343 4C-D left). These experiments employ the cross-polarization (CP) technique, which
344 means that the observable residues must be rigid or immobilized, lacking high flexibility
345 [40]. This conclusion is reinforced by a lack of signals in INEPT-based ssNMR spectra that
346 are selective for highly dynamic peptide segments [41-43] (more below). Then, the observed
347 narrow signals must originate from an immobilized, well-ordered subset of DnaJB8
348 residues. Based on the characteristic NMR shifts of amino acid types (Supplementary
349 Figure 4A)[44], we can attribute these narrow signals to residues in the JD (Table 1) while
350 the broad peaks are dominated by signals from residues common in other domains (Table
351 1). The narrow signals reflect mostly α-helical structure, unlike the broader signals that

352 are mostly random coil and β-sheet [45]. Finally, with known chemical shifts of the DnaJB8
353 JD in solution (see also below), we prepared a synthetic 2D spectrum (Supplementary
354 Figure 4B) that reveals a striking correspondence to the narrow ssNMR peaks (Figure
355 4C-D). The correspondence is such that we tentatively assign the strikingly narrow
356 signals (Supplementary Figure 4A,B) to residues in helix 2 and helix 3 (10V, 13S, 14A,
357 15S, 19I, 22A, 27A, 42A, 52A). In absence of experimental solution NMR data for the
358 other domains, we predicted estimated spectra based on their model structures. Figure
359 4C-D (green) shows Ala and Ser regions of their combined simulated NMR spectrum[46],
360 resembling qualitatively the broader signals in our 2D ssNMR data. A particular strength
361 of MAS ssNMR analyses of such hydrated proteins is the ability to gauge local and global
362 dynamics. Single pulse excitation (SPE) and refocused INEPT ssNMR spectra, which
363 enhance the more dynamic parts of samples[42-43], show surprisingly little evidence of
364 flexible residues (Figure 4E red). The main INEPT signal at ~42ppm arises from Lys side
365 chains, which are expected to be solvent exposed and dynamic. Since the 1D CP and
366 SPE spectra look similar, with higher signal intensities in the former, the different domains
367 of the protein must have a similar degree of mobility (Fig. 4E). Combined, the ssNMR
368 data reveal oligomers that are heterogeneous in structure but lack extended flexible
369 domains. In other words, the central F/G and ST domains are heterogenous, but also
370 substantially immobilized within the oligomers. Uniquely ordered are parts of the JD
371 (residues in helices 2 and 3), which appear to be well-folded and immobilized.
372
373 **Interaction sites from ssNMR**
374 In the JD structure (Figure 4F-I) these "ordered" residues form a surface region rich in
375 positively charged amino acids, involving helix 2 and 3, as well as residues connecting
376 these helices. What is responsible for stabilizing and immobilizing this part of the JD? XL-
377 MS showed long-range contacts from the JD to the CTD, involving K34, K47, and K60 in
378 helices 2, 3 and 4, which disappeared at elevated ionic strengths. Analogous ssNMR
379 studies of the oligomers in PBS buffer with 285mM NaCl are shown in Fig. 4B and S4.
380 The 2D CP-based ssNMR spectrum reproduces the broad signals of the immobilized

381 oligomers, but the narrow JD peaks are strikingly absent. Comparing the CP and SPE
382 ssNMR spectra (Figure 4E), there is a clear increase in mobility, but again there is a lack
383 of INEPT signals from highly flexible regions. Notably, although the well-ordered JD
384 signals are no longer seen as immobilized (i.e., visible in CP ssNMR), no new "flexible"
385 ssNMR signals were identified under high salt conditions. We interpret this as indicating
386 that the JD gains increased mobility due to disruption of its long-range electrostatic
387 interactions but is still folded and partly immobilized by its covalent attachment to the
388 overall assembly. As a consequence, the JD is invisible due to intermediate timescale
389 dynamics[40, 47]. Since the broad signals from the other domains are preserved, it appears
390 that the core architecture of the oligomers persists even at high ionic strength, such that
391 it is primarily the JD that is dislodged as electrostatic long-range interactions are
392 weakened.
393
394 **Isolated JD and CTD are folded and monomeric**
395 To evaluate the potential inter- and intra-domain interactions of the JD and CTD, we
396 produced isolated JD (residues 1-77; JD_{1-77}) and CTD (residues 170-232; $CTD_{170-232}$)
397 (Figure 5A). By size exclusion chromatography (SEC) both constructs yielded
398 monodisperse peaks (Figure 5B), with an estimated molecular weight of 10kDa and 8kDa
399 for JD_{1-77} and $CTD_{170-232}$, respectively. The CTD has been proposed to drive dimerization
400 and multimerization in the homologous DnaJB6b[24-25], but by Size Exclusion
401 Chromatography - Multi Angle Light Scattering (SEC-MALS) the molecular weight for the
402 DnaJB8 $CTD_{170-232}$ is unambiguously a monomer with a molecular weight of 8,376±14
403 g/mol (Supplementary Figure 5A). Also, by DLS in solution we estimated the JD_{1-77} to be
404 2.30±0.12 nm and the $CTD_{170-232}$ to be 1.71±0.02 nm, with both stable over 15 hours
405 (Supplementary Figure 5B, Supplementary Data 3). The purified constructs were used
406 for XL-MS to probe the structural similarities to the corresponding domains within the full-
407 length protein. On an SDS-PAGE gel, the crosslinked JD_{1-77} and $CTD_{170-232}$ remained
408 monomeric following crosslinking, while the bands broadened as a result of the chemical
409 modification (Figure 5C). XL-MS analysis yielded 4 crosslinks for JD_{1-77} and 6 crosslinks

410 for $CTD_{170-232}$ (Figure 5D, Supplementary Data 2). The identified crosslinks revealed good
411 agreement between the local domain crosslinks observed in the full-length DnaJB8 and
412 the isolated JD_{1-77} and to a lesser extent for $CTD_{170-232}$ (Figure 5D, S5C-D).
413 We built 5000 predictive models of the CTD using *ab initio* ROSETTA which
414 employed fragment libraries derived from experimental structures[40]. We calculated the R_h
415 for the ensemble using HYDROPPRO and the resulting values were consistent with the
416 DLS measurement of 1.7nm (Figure 5E). The models reproducibly formed a low contact
417 order 5-stranded β-sheet topology (Figure 5E) and the R_h variation can be attributed to
418 the more flexible termini (Figure 5E, inset). The CTD topology is defined by four β-turns
419 stabilized by conserved asparagine/aspartate-glycine sequences (N/DG). These
420 structures are consistent with the recently published conformation of the DnaJB6b CTD[23].
421 Circular dichroism (CD) on the CTD sample yields spectra consistent with a
422 predominantly β-sheet content, as predicted by our model (Supplementary Figure 7E-F).
423 We mapped the 14 CTD-derived crosslinks from across experiments onto the monomeric
424 ensemble, finding that a majority of structures explain 10-11 crosslinks but only a single
425 model explains 13 of 14 (Figure 5F). These crosslink pairs map onto each face of the β-
426 sheet and the distances are compatible with the geometry of the crosslinking chemistry.
427 The crosslinks that fall outside of the distance cutoff localize to the more dynamic C-
428 terminus of CTD (Figure 5E, inset) at positions K227 and K223 (Figure 5F). Thus, our
429 data support that both the JD_{1-77} and $CTD_{170-232}$ domains are folded, monomeric and do
430 not have intrinsic assembly properties.
431
432 **Basic surface on JD drives interaction with CTD**
433 In our experiments on the full-length DnaJB8 oligomers we saw that the JD and CTD
434 interact through complementary electrostatic surfaces. We further probed this interaction
435 by mixing the individual JD_{1-77} and $CTD_{170-232}$ domains *in vitro* (Figure 6A). We incubated
436 Flourescein(FITC)-labelled JD_{1-77} with a series of $CTD_{170-232}$ concentrations and
437 measured binding affinity using a fluorescence polarization assay. The resulting binding
438 curve revealed that the JD_{1-77} binds to the $CTD_{170-232}$ with 0.575±0.115 μM affinity (Figure

439 6B). Preincubated JD_{1-77} and $CTD_{170-232}$ domains were crosslinked with ADH/DMTMM
440 and analyzed using XL-MS. We identified local crosslinked pairs consistent with pairs
441 observed in full length DnaJB8 and the isolated JD_{1-77} and $CTD_{170-232}$ samples (Figure
442 6C). Importantly, we also reconstitute intermolecular contacts between the JD_{1-77} and
443 $CTD_{170-232}$ observed in full length DnaJB8 experiments. However, an increased variance
444 in the crosslink profile may indicate that the missing proximal sequences help define the
445 proper architecture of the full-length DnaJB8 oligomers. Solution NMR-based chemical
446 shift mapping was used to identify the JD_{1-77} surface that interacts with the $CTD_{170-232}$
447 (Figure 6D). Titration of increasing amounts of unlabeled $CTD_{170-232}$ into ^{15}N-labeled JD_{1-}
448 $_{77}$ produced concentration-dependent shifts in a specific subset of peaks (Figure 6D-E);
449 33 peaks were strongly perturbed (>0.2 p.p.m.) and another 40 peaks were perturbed
450 weakly (>0.1 p.p.m; Fig 6F). Among the strongly perturbed peaks, 27 residues have
451 solvent accessible side chains of which fifteen are charged, with a notable overlap with
452 the basic face in helix 2 that is implicated in Hsp70 binding (Figure 6H-I). Other residues
453 that show strong perturbations are basic and acidic residues that wrap around the exterior
454 face of the JD loop and helix 3 (D33, K39, E40, E41, K44, K47, E51), and residues on
455 the charged face of helix 4 (K60, K61, R62, L64, Y65). While a few other hydrophobic
456 residues also show strong perturbations, all are in close proximity to charged residues
457 along each helix. Given the small size of the JD_{1-77}, it is likely that residues in the core
458 behind the basic surface involved in the interaction experience chemical shifts.
459
460 **Sequence properties driving interactions in DnaJB8**
461 Using Rosetta, we generated a full-length model of DnaJB8 combining the solution NMR
462 structure of the JD (PDBID: 2DMX) with the *ab initio* model for CTD while keeping the
463 F/G and S/T region expanded. Using the relax module in Rosetta we applied our JD-
464 CTD XL-MS crosslink pairs as constraints to collapse the expanded full-length DnaJB8
465 monomer (Figure 7A and Supplementary Figure 7A). The constraints drive the collapse
466 of the molecule to decrease the distance between the crosslink pairs (Figure 7A and
467 Supplementary Figure 7A) from an R_g of 6.65 nm in the expanded state to a much smaller

468 2.45 nm (Figure 7C and Supplementary Figure 7B). Using the Hydropro software[48], we
469 obtain R_h values of 9.27 nm and 4.02 nm, respectively, for each structural model.
470 Comparing the DLS R_h size ranges for the small species in the low and high ionic strength
471 conditions to the structure-derived R_h values suggests congruency in observed shapes
472 dependent on presence or absence of JD:CTD contacts. The calculated R_h values for the
473 collapsed (JD:CTD engaged) Rosetta monomer conformation is consistent with the lower
474 end DLS size distribution obtained under low ionic strength. This is further supported by
475 comparing the R_h of our Rosetta model to a theoretical disordered protein containing 232
476 amino acids to be 3.98 nm as modeled by Marsh and Forman-Kay[49]. We calculated the
477 spherical volume of our collapsed model to be 271.78 nm^3. By using this smaller sphere
478 and fitting multiple copies of it into the predicted volumes for larger oligomeric species,
479 we estimate that the small species range from a monomer to 8-mer under low ionic
480 strength conditions, which over time assemble into larger polydisperse species.
481 Guided by the constraints, the final model "docks" the JD onto the CTD placing the
482 putative acidic surface on the CTD (E208-D212) in contact with the NMR-identified basic
483 surface on the JD (K20-R29) (Figure 7A and Supplementary Figure 7B). The final model
484 also docks Helix 5 onto the JD:CTD interface (Figure 7A). The CTD has proximal basic
485 surfaces that flank the acidic surface, generating a characteristic alternating charge
486 pattern that is inverted on the JD (Figure 7B). Furthermore, in the collapsed monomer,
487 the 17 aromatic residues distributed in the F/G and S/T regions are exposed to solvent
488 highlighting their possible role in oligomerization (Figure 7A). Although the NMR results
489 were not employed as constraints, it is striking that the predicted interaction sites line up
490 well with the solution and solid-state NMR data. These simulations, in conjunction with
491 our ionic strength perturbation experiments support a model in which the JD-CTD
492 interaction is coupled to the conformation of the F/G and S/T region with the potential to
493 sense substrate binding and modulating the oligomer assembly.
494
495 **Evolutionary preservation and co-evolution**

496 If this interaction has biological relevance, we may expect it to be evolutionarily preserved.
497 To probe this, we computed the extent of conservation across DnaJB8 homologs
498 (Supplementary Figure 7C). The JD is the most conserved domain. Particularly for
499 DnaJB6b, DnaJB2 and DnaJB7 homologs which also encode a five-stranded pleated β-
500 sheet CTD, we found specific sites on the CTD with an elevated degree of conservation,
501 these residues map to the N/D-G β-turns and the β-sheet surface of the CTD
502 (Supplementary Figure 7D). In the Rosetta-generated model, the majority of these
503 conserved CTD sites are participating in the JD-CTD interface (Supplementary Figure
504 7D-E). A similar sequence analysis for the homologous DnaJB6b sequence reveals
505 similar conservation patterns and charge distributions (Supplementary Figure 7F). This
506 supports the idea that the JD-CTD interaction has a degree of conservation across DnaJ
507 sequences featuring homologous CTD-like domains.
508
509 Lastly, we incorporated co-evolution analysis using the Gremlin algorithm[50-52]. Employing
510 an alignment of DnaJB8 homologs we identified amino acid positions that covary,
511 restricting analysis to only pairs showing >70% probability of being in contact. While many
512 of the amino acid pairs covary within the JD and CTD domains, we additionally observe
513 pairs that reflect inter-domain contacts between the JD-CTD (Figure 7C). Comparison of
514 these long-range covariance sites reveals a striking resemblance to the XL-MS pairs
515 identified in the full length DnaJB8 experiments. The similarity between the predicted
516 covarying contacts (Figure 7C), conservation (Supplementary Figure 7C-D) and the XL-
517 MS experimental contacts not only further strengthens our DnaJB8 JD-CTD model, but it
518 also suggests that XL-MS can detect functionally important yet lower affinity interaction
519 sites.
520
521 **JD-CTD interaction competes with Hsp70 binding**
522 The conserved Hsp70-JD electrostatic contacts (Figure 1) that overlap with the JD-CTD
523 contact sites lead us to hypothesize that the observed JD-CTD interactions could regulate
524 the recruitment of Hsp70 (Figure 8A-B). To test this hypothesis, we employed a

525 competition experiment leveraging a fluorescence polarization binding assay to
526 discriminate the JD-CTD and JD-HspA1A interactions (Figure 8C). For the JD:HspA1A
527 titration we determine a binding constant of 0.257±0.029μM, consistent with values
528 observed in the literature[53] and similar to the JD:CTD interaction (Figure 8D, black and
529 green, respectively). Due to the large size difference of HspA1A (70 kDa) and the CTD
530 (8.7 kDa) the respective titrations saturate at different polarization values (Supplementary
531 Figure 8A, black and green, respectively). Leveraging this signal difference, we designed
532 an experiment to measure the competition of HspA1A and CTD binding to the JD. We
533 preincubated the FITC-labeled JD with a fixed concentration of CTD (3.125 μM) and then
534 subsequently titrated increasing concentrations of HspA1A. The polarization signal was
535 consistent with the already measured CTD-JD complex, up until HspA1A concentrations
536 reached 3.125uM. Past this point, the signal more closely matched that seen for the larger
537 HspA1A-JD complex (Supplementary Figure 8A, purple). Normalization of the
538 polarization data reveals a ~25-fold shift in the apparent binding constant between
539 JD:HspA1A when preincubated with CTD (Figure 8D). XL-MS using ADH/DMTMM was
540 used to identify contact points between the JD and HspA1A, revealing 3 zero-length
541 cross-links (K41-E513, K51-D323, and D65-K319) that are all consistent with the
542 structural model of the JD_{1-77}-HspA1A interaction (Figure 8E, Supplementary Data 2).
543 Consistent with our findings in cells (above), incubation of HspA1A with full-length
544 DnaJB8 yielded intra-molecular cross-links for DnaJB8 and HspA1A, but no
545 intermolecular cross-links observed between the two different proteins (Supplementary
546 Data 2). Thus, the DnaJB8 JD uses the same basic surface to bind to its own CTD and
547 HspA1A. Based on our DLS data and Rosetta models of DnaJB8, the oligomer shape
548 changes with the engagement of the JD:CTD interaction. When the JD:CTD interaction
549 is preserved, DnaJB8 is capable of forming species ranging from monomer to octamer,
550 which proceed to larger oligomers over time (Figure 8F). The disruption of this JD:CTD
551 interaction liberates the HspA1A binding face of the JD and reduces the oligomer size to
552 a more uniform size. Considering the possible role of substrates, our model proposes that
553 *in vivo* it is the binding of Hsp40 client peptides and proteins that acts as the driving force

554 that disrupts the DnaJB8 oligomer and the JD:CTD interaction, thus promoting HspA1A
555 recruitment for substrate transfer. This then represents an exciting new regulatory
556 mechanism by which Hsp40s orchestrate the recruitment of Hsp70 (Figure 8F).
557

558 DISCUSSION
559

560 **Structure and dynamics of oligomeric DnaJB8**

561 Using a hybrid structural approach, we described the key molecular interactions in the
562 oligomeric state of the Hsp40 co-chaperone DnaJB8. By DLS and TEM, we observed that
563 DnaJB8 forms oligomers that vary in size and shape. In cells, DnaJB8 forms small puncta
564 consistent with the size of our *in vitro* produced aggregates. We used XL-MS to capture
565 surface contacts within and between folded domains and saw that they were similar *in*
566 *vitro* and in cells. Independent of the conditions, the protein assembled into oligomeric
567 base units with a R_h range of ~4-8 nm, which is consistent with an assembly of at most
568 eight monomers. Under normal ionic buffer conditions these assembles mature into larger
569 polydisperse assemblies while in the presence of higher salt they stable. The collective
570 data reveal that the core of these assemblies is formed by immobilized F/G and S/T
571 domains, while the JD and CTD are engaged in electrostatic interactions at the surface
572 rendering them sensitive to changes in ionic strength (Figure 8F). With ssNMR of the
573 assembled oligomers, we showed that the F/G and S/T domains lack secondary structure,
574 consistent with computational predictions, but should not be seen as dynamic, flexible
575 regions in the oligomers. Dynamics-sensitive ssNMR instead showed them to be
576 immobilized and insensitive to the destabilizing effects of elevated ionic strength. We
577 propose a model in which self-assembly of these oligomer cores is driven by hydrophobic
578 clustering and pi-pi stacking of aromatic side chains in the F/G and S/T domains (Figure
579 8F). At the periphery of this hydrophobic core are charged and hydrophilic residues, with
580 the former engaged in electrostatic interactions that are critical for the DnaJB8 self-
581 assembly and function.
582

583 We combined a variety of XL-MS and NMR in the solid and solution states to probe these
584 inter-domain interactions. One of the most striking features was a newly identified
585 interaction between the distal JD and CTD driven by electrostatics, whose perturbation
586 had a dramatic effect on the structure, dynamics and higher order assembly of the
587 oligomers. Analysis of the isolated JD and CTD showed a reduced mutual interaction,
588 revealing a distinct role for the intervening domains. Indeed, our data argue that the S/T
589 and F/G domains are central in the homo-oligomerization process, as the isolated JD and
590 CTD are surprisingly resistant to self-assembly. These findings are distinct from published
591 reports on the otherwise highly homologous DnaJB6b. The modeled structure of the CTD
592 is however very similar to its DnaJB6b counterpart, featuring a pleated β-sheet topology
593 absent of a hydrophobic core[23]. Consistent with prior observations from solution NMR
594 data we also observe weak contacts between the JD and a downstream helix in the FG
595 domain, similarly based on electrostatics. Supporting an electrostatically driven
596 immobilization of the JD, ssNMR analysis showed the JD mobility to be dependent on the
597 ionic strength. Thus, we conclude that the JD is bound to charged groups on the
598 oligomers' surface.
599
600 **Functional role of the CTD in the oligomeric co-chaperones**
601 Multiple analyses reveal the isolated DnaJB8 CTD to be a monomer encoding a five-
602 stranded pleated β-sheet topology. Our structural models for the DnaJB8 CTD are in
603 agreement with recent cs-Rosetta simulations on the DnaJB6b CTD[23]. This topology
604 resembles the negatively charged β-sheet surface on Hsp70 that is known to interact with
605 the JD[16]. Interestingly, outside of inter-strand hydrogen bonding and polar side-chain
606 contacts, it is not clear what forces stabilize this domain. This may explain the apparent
607 CTD heterogeneity (unlike the JD) seen in the ssNMR spectra. In DnaJB6b the CTD itself
608 has been implicated in driving the assembly of oligomers, even though the literature has
609 conflicting results[22-24, 26]. Söderberg *et al* have proposed that the minimal assembly is a
610 dimer mediated by inter-CTD contacts[25]. A recent solution NMR study showed that
611 truncating the entire S/T region or partial truncation of the CTD blocks oligomerization[23].

612 Our data show that the DnaJB8 CTD is not prone to dimer formation, presumably implying
613 a need for the other DnaJB8 domains. Considering the size of the DnaJB8 oligomeric
614 assembly, the inability of the CTD to self-assemble indicates that this domain alone is not
615 the driving force behind DnaJB8 oligomerization. While more experiments are required,
616 our data suggest a possible alternate mechanism where the JD-CTD interaction is
617 coupled strongly to the disordered F/G and S/T domains, with them together modulating
618 oligomerization. Mimicking the effect of ionic strength modulation, it is worth noting that
619 the lysines in the DnaJB8 and DnaJB6b CTD can be acetylated and deacetylated (via
620 Histone Deacetylases (HDACs)) to modify these proteins' self-assembly and function[22,
621 26]. The CTD architecture is conserved in a subset of B family member Hsp40s including
622 DnaJB2, DnaJB6b, and DnaJB7, of which DnaJB6b has also been shown to oligomerize.
623 It is tempting to speculate that the CTD in these DnaJB family members similarly serves
624 a regulatory role in which post-translational modifications could alter the affinity for the
625 JD, and thus indirectly alters assembly properties or Hsp70 recruitment.
626

627 **Implications for Hsp70 recruitment and substrate binding.**

628 DnaJB8 is responsible for the recognition and binding of particular misfolded substrates
629 such as expanded polyglutamine domains and Aβ[22,26-27,39]. Aside from inhibiting
630 aggregation on its own, DnaJB8 also recruits Hsp70 for further processing of bound
631 substrates. This necessitates a mechanism that connects Hsp70 recruitment to substrate
632 recognition and binding. Our current findings offer a potential molecular rationale,
633 involving auto-inhibitory interactions of the Hsp70-binding JDs within the DnaJB8 native
634 oligomer state. The recently solved structure of the JD of DnaJ in complex with DnaK·ATP
635 showed that the JD binds between the NBD and SBDβ domains of DnaK[16]. The
636 interaction surface is characterized by charge complementarity, involving a highly
637 negative side of DnaK and a highly positive region of the JD. The bacterial protein
638 interface is recapitulated in our modeling of HspA1A and the DnaJB8 JD (Figure 8B-C).
639 This involves residues involved in the DnaJB8 JD-CTD interactions, explaining the lack
640 of Hsp70 recruitment by oligomeric DnaJB8 in cells and *in vitro*. This is validated by the

641 observed competition between Hsp70 and CTD binding to the JD (Figure 8F). In terms of
642 the functional mechanism of DnaJB8 substrate recognition and Hsp70 recruitment, we
643 propose the following mechanism based on these findings.
644
645 In the non-stressed native state, the DnaJB8 forms oligomers in which the JD is engaged
646 in electrostatic interactions and thus not available for very effective Hsp70 binding.
647 Substrate binding to DnaJB8 is expected to disrupt the normal state of the oligomer
648 complex and could cause the release of the immobilized JD (in a manner analogous to
649 the ionic strength experiments). As a consequence, the Hsp70-binding helix-turn-helix
650 motif of the JD becomes available. This would enable the recruitment of Hsp70 to the
651 loaded DnaJB8 protein (Figure 8F). The substrate could do so by disrupting the oligomer
652 structure altogether. However, our data illustrate that complete loss of the oligomers is
653 not required for a mobilization of the JD. The oligomers must be stabilized by self-self
654 interactions that are not disrupted by ionic strength, and do not require the involvement
655 of the JD. We propose that the more hydrophobic F/G domain may form this salt-resistant
656 core structure, with the CTD and JD being more surface exposed. Thus, it may be
657 possible to recruit Hsp70 to an oligomeric state of DnaJB8, without a need for complete
658 solubilization of the protein. Although we employed ionic strength to manipulate the
659 sequestration of the JD helix-turn-helix motif, it is tempting to speculate that this could
660 also be affected by changes in the S/T and/or F/G domains. Here, it is noteworthy that
661 negative residues in helix 5 (E97/D98) in the F/G domain interact with the JD (XL-MS
662 data). A disruption of the JD-CTD interaction may therefore be coupled to low complexity
663 sequences located in the S/T domain that are thought to mediate substrate binding.
664 Future mechanistic and structural studies on this complex co-chaperone with substrates
665 will reveal the interplay between oligomer dynamics, substrate binding and recruitment of
666 Hsp70.
667

668 CONCLUSIONS

669 We present a hybrid structural biology studies of DnaJB8 oligomers to reveal a new role
670 for specific electrostatic contacts that mediate the homo-oligomeric assembly *in vitro* and
671 *in vivo*. Despite a heterogeneous structure of the oligomers, our use of complementary
672 XL-MS, (ss)NMR studies and *in silico* analyses provided a novel perspective on the
673 fundamental structure of the protein complex and its function. We show an exciting
674 interplay between contacts that drive self-assembly and regulate recruitment of Hsp70 to
675 the JD, pointing to an orchestrated auto-inhibitory mechanism involving the latter. Future
676 studies will be focused on the interplay between DnaJB8 conformation, substrate binding,
677 and Hsp70 recruitment. This study highlights how hybrid structural methods can reveal
678 novel insight in a dynamic and polydisperse oligomeric chaperone.
679

680 MATERIALS AND METHODS

681

682 **Sequence and structural analysis**

683 Analysis of protein sequences was performed using Local CIDER[54]. Secondary structure
684 prediction was calculated using PSIPRED[31-32] and the extent of disorder was calculated
685 using DISOPRED[55]. An ensemble of 5000 HspA1A structural models was produced using
686 *ab initio* Rosetta using the DnaK (PDB:5NRO) conformation as a template[16]. Briefly, the
687 HspA1A sequence was aligned to the DnaK sequence to identify regions with loop
688 insertions and deletions. The HspA1A fragment library was produced using the fragment
689 picker. The lowest scoring model was used to produce a complex between HspA1A and
690 the DnaJB8 JD. The structural images were produced using PyMOL.
691

692 **Cell biological and biochemical analysis of DnaJB8-Clover cell lines**

693 The human *DNAJB8* protein-coding sequence was cloned using Gibson assembly into a
694 modified FM5 lentiviral expression plasmid[56] in which the *UbC* promoter was replaced by
695 a *CMV* promoter, the linker sequence was replaced by "GSAGSAAGSGEF" and
696 the *YFP* was replaced by *mClover3*. The resulting gene produced a DNAJB8-mClover3
697 fusion protein. In parallel, we produced a construct that expresses the fluorescent protein

698 (mClover3) but lacks DNAJB8. Both plasmids we separately co-transfected into HEK293T
699 cells along with helper plasmids (pCMV-VSV-G and psPAX2) to produce lentivirus, which
700 was harvested after 48hrs and used to produce polyclonal cell lines that expressed either
701 DNAJB8-mClover3 or mClover3. For crosslinking experiments, cells from a confluent
702 10cm^2 cell culture dish were pelleted and lysed using an insulin syringe in 1xPBS with
703 1mM DTT, 1mM PMSF, 1x EDTA-free Protease Inhibitor Cocktail (Roche), and 1%
704 Digitonin. After spinning at 1000xg for 10min., the lysate was recovered and incubated
705 with a polyhistidine tagged GFP-nanobody (purified as described previously[34]) for 2.5
706 hours at 4ºC. The lysate was then incubated with 25µL NiNTA beads (Clontech) (for 1
707 hour at 4ºC for binding. The beads were washed five times with 300µL 1xPBS. The buffer
708 for each wash was removed after pulse spinning the beads via centrifugation. The beads
709 were preincubated for 5 minutes at 37ºC and a final concentration of 57mM ADH and
710 36mM DMTMM were added to each sample. Following a one-minute incubation with
711 chemical crosslinkers, the reaction was quenched with 1mM ammonium bicarbonate.
712 After another pulse spin to remove the buffer, the beads were resuspended in elution
713 buffer, (8M Urea, 0.5M imidazole, pH 7.5). After a final pulse spin, the supernatant was
714 retained and analyzed by mass spectrometry.
715

716 **Analysis of Mass Spectrometry Results**

717 Each Thermo .raw file was converted to .mzXML format for analysis using an in-house
718 installation of xQuest[57]. Score thresholds were set through xProphet[57], which uses a
719 target/decoy model. The search parameters were set as follows. For grouping light and
720 heavy scans (hydrazide crosslinks only): Precursor mass difference for isotope-labeled
721 hydrazides = 8.05021 Da for ADH-d_0/d_8; maximum retention time difference for
722 light/heavy pairs = 2.5 min. Maximum number of missed cleavages = 2, peptide length =
723 5-50 residues, fixed modifications = carbamidomethyl-Cys (mass shift = 57.02146 Da),
724 mass shift of light crosslinker = 138.09055, mass shift of monolinks = 156.1011 Da, MS^1
725 tolerance = 15 ppm, and MS^2 tolerance = 0.2 Da for common ions and 0.3 Da for crosslink
726 ions; search in enumeration mode. For zero-length crosslink search: maximum number
727 of missed cleavages = 2, peptide length = 5-50 residues, fixed modifications
728 carbamidomethyl-Cys (mass shift = 57.02146 Da), mass shift of crosslinker = -18.010595
729 Da, no monolink mass specified, MS^1 tolerance = 15 ppm, and MS^2 tolerance = 0.2 Da

730 for common ions and 0.3 Da for crosslink ions; search in enumeration mode. The FDRs
731 of all *in vitro* experiments range from 0.05 to 0.33.
732
733
734 **Western blot analysis**
735 10µL aliquots of the HEK control, Clover, and DnaJB8-Clover cell-lines were removed
736 from the elution and loaded onto a 4-12% Bis-Tris SDS-PAGE gel for western blotting.
737 Upon running the gel to completion, the gel transferred onto a transfer membrane soaked
738 in Novoblot transfer buffer. Following the transfer, the membrane was soaked in milk
739 blocking buffer for 1 hour at room temperature. For immunolabelling, we added 1:2000
740 dilution of polyclonal Anti-GFP (rabbit) (Rockland) in milk and incubated the membrane
741 shaking at room temperature for 2 hours. The primary antibody solution was dumped and
742 the membrane washed three times for 10 minutes each with 1xTBST before adding the
743 polyclonal Anti-Rabbit Peroxidase (Rockland) at a 1:5000 dilution in milk. The membrane
744 was incubated with secondary antibody at room temperature for 1 hour before removing
745 the antibody solution. The membrane was washed 3 times in 5-minute intervals with
746 1xTBST and finally one 5-minute wash with 1xTBS. The membrane was soaked in 1mL
747 of Luminol enhancer and peroxide solution for 1 minute before imaging.
748
749 **In cell analysis of DnaJB8-Clover and Clover cell lines**
750 HEK293T cells expressing either DNAJB8-mClover3 or mClover alone were plated at
751 300,000 cells per well in media (10%FBS, 1%Pen/Strep, 1%GlutaMax in DMEM) in a 6-
752 well glass bottom plate (Cellvis, P06-1.5-N). After 30 hours, cells were stained with
753 Hoescht33342 at a final concentration of 2ug/mL in cell media for 30 minutes at 37C and
754 5%CO2. The plate was placed on an InCell6000 with a heated stage and fifty fields of
755 view were imaged under DAPI and FITC channels at 60X magnification (Nikon 60X/0.95,
756 Plan Apo, Corr Collar 0.11-0.23, CFI/60 lambda). Images were exported as TIFF files for
757 downstream analysis.
758

759 **Identification of factors bound to DnaJB8**

760 DnaJB8-Clover was purified from HEK293 cells as described previously[34] using a GFP-
761 nanobody construct with a His tag. The pulldown was analyzed via LC-MS/MS, resulting
762 in mass spectra with mass peaks for all proteins in solution. The resulting data was
763 submitted to the CPFP[35] server for peak assignment and protein identification. The UTSW
764 CPFP server assigns protein peptides to peaks in submitted mass spectra by searching
765 the NCBI and EBI protein databases for mass spectra matches to known protein
766 sequences. The output results assign each identified protein a value in sequence
767 coverage, peptide-spectrum match (PSM), unique peptide hits, and matched isotope
768 pattern chromatograms (MICs). Using a Clover only cell line as a control, we compared
769 MIC scores for relative protein abundance in the DnaJB8-Clover sample to determine
770 which proteins were more abundant in the presence of DnaJB8 during the pulldown and
771 used sequence coverages >70% and PSMs>50 to restrict the list. Hits identified in the
772 DnaJB8-Clover pull downs that were enriched relative to the Clover controls were input
773 into the string database[58] to build network interaction maps based on interactions
774 described in the literature.

775

776 **Recombinant expression and purification of DnaJB8**

777 The vector used for DnaJB8 expression was a pET-29b vector containing the gene for
778 human DnaJB8, a T7 promoter to activate DnaJB8 expression, a His tag region at the
779 end of the gene, and a gene for kanamycin resistance. This vector construct was
780 transformed into *E. coli* BL-21 (DE3) cells and plated onto 2xLB plates containing
781 0.05mg/mL Kanamycin. 12mL of 2xLB, 0.05mg/mL Kanamycin were prepared and
782 inoculated with a single colony from the plate. This small culture was incubated overnight
783 at 37°C while shaking at 220rpm. In the morning, the 12mL culture was added to 1L of
784 2xLB supplemented with 0.05mg/mL Kanomycin and incubated at 37°C while shaking at
785 220rpm. Once OD600 reached 0.6-0.8 A.U., 1mL of 1M IPTG was added to induce
786 DnaJB8 expression. After incubation for an additional 4 hours, the cells were harvested
787 by spinning down the culture at 4,000g for 20 minutes.

788 The resulting cell pellet was resuspended in 25mL 1xPBS and 1mM PMSF in preparation
789 for insoluble separation. The resuspended cells were sonicated at 30% power, 5X pulse
790 for 10 minutes using an Omni Sonic Ruptor 4000 (Omni International). The lysed cells
791 were pelleted at 10,000g for 30 minutes and the supernatant was discarded. The
792 insoluble pellet was rinsed with 1xPBS, 0.75%Tween-20 and again pelleted at 10,000g
793 for 30 minutes.
794 The insoluble cell pellet was resuspended in 50mL lysis buffer (8M Guanidinium HCl,
795 50mM HEPES, 20mM Imidazole, 1mM DTT pH 7.5) and sonicated at 30% power, 3X
796 pulse for 1 minute to solubilize the DnaJB8 from the insoluble pellet. After a 30-minute
797 incubation at room temperature, the cellular debris was pelleted at 15,000g for 30
798 minutes. The resulting supernatant was mixed with 2mL HisPur™ Ni-NTA Resin (Thermo
799 Scientific) for 1 hour before being loaded onto a gravity column. The column was washed
800 with an additional 50mL of lysis buffer, followed by 50mL of a second wash buffer (50mM
801 HEPES, 20mM Imidazole, 1mM DTT pH 7.5 in H_2O). The protein was eluted with 30mL
802 of elution buffer (50mM HEPES, 500mM Imidazole, 1mM DTT pH 7.5 in H_2O) and
803 collected in 2mL fractions. After selecting for fractions with high purity, the DnaJB8
804 solution was loaded into 3.5kDa cutoff Biotech CE Dialysis Tubing (Spectrum Labs) and
805 dialyzed overnight at 4ºC in 50mM ammonium formate to minimize assembly. The protein
806 was then lyophilized and stored at -80°C for future use.
807
808 **Dynamic Light Scattering**
809 All samples were prepared at 1.2mg/mL in 1xPBS, 1mM DTT, pH 7.4. All protein samples
810 were filtered through a 0.22µm PES sterile filter and loaded in triplicate onto a 384 well
811 clear flat-bottom plate. The plate was loaded into a Wyatt DynaPro Plate Reader III and
812 set to run continuously at room temperature at a scanning rate of 1 scan per 15 minutes,
813 with 1 scan composed of 10 acquisitions. The data were analyzed using the Wyatt
814 Dynamics software version 7.8.2.18. Light scattering results were filtered by Sum of
815 Squares (SOS) <20 to eliminate statistical outlier acquisitions within each scan. For
816 DnaJB8 in 1xPBS(150mM) buffer, one of the triplicates contains partial data due to high

817 SOS values. This is a result of increasing polydispersity and heterogeneity, which is
818 consistent with oligomers of that size. Average R_h readings at each time point were
819 reported and further averaged across triplicate wells. Data for the smallest particles was
820 reported by filtering out any signal that was greater than 10nm for runs with JD_{1-77} and
821 $CTD_{170-232}$, while more broad analyses such as the full DnaJB8 protein did not consider
822 size cutoffs.
823
824 **Transmission Electron Microscopy**
825 5µL of sample at 200µM was loaded onto grids. 200 mesh formvar grids are prepared
826 through glow discharge followed by the application of each 5µL sample onto each grid.
827 After 30 seconds, the grid is blotted by filter paper followed by washing the grid with 5µL
828 of ddH_2O. After another 30 seconds, the grid is blotted again followed by the addition of
829 5µL of 2% uranyl acetate for negative staining. After 1 minute, the grid was dried for the
830 final time and loaded into a FEI Tecnai G2 Spirit Biotwin TEM. All images were captured
831 using a Gatan 2Kx2K multiport readout post column CCD. The images were acquired at
832 the UT Southwestern EM Core Facility.
833
834 **Cross-Linking Reagents**
835 All crosslinking reagents used are commercially available: ADH (Sigma-Aldrich), and
836 mixed light and deuterated ADH (ADH-h_8/d_8) (Creative Molecules). DMTMM (Sigma-
837 Aldrich). For all crosslinking experiments, stock solutions were made of each crosslinking
838 reagent. A 1:1 ADH-d_0/ADH-d_8 solution was made at 100mg/mL in 1xPBS pH 7.4 (Sigma-
839 Aldrich). DMTMM (Sigma-Aldrich) was prepared at a 120mg/mL concentration in 1xPBS
840 pH 7.
841
842 **Cross-Linking Mass Spectrometry**
843 The *ex-vivo* purified DnaJB8 was dialyzed to remove excess imidazole, and transferred
844 into 1xPBS pH 7.4 buffer. For the full-length DnaJB8 experiments, lyophilized DnaJB8
845 was resuspended in either 1xPBS(150mM) or 1xPBS(285mM) to a concentration of

846 100µM. The JD_{1-77} and $CTD_{170-232}$ constructs were purified into 1xPBS buffer, and were
847 prepared for XLMS experiments at 100µM each. 2µM HspA1A in 1xPBS pH 7.4 buffer
848 and mixed with either 40µM DnaJB8 or 40µM JD_{1-77} for XLMS experiments. All samples
849 were incubated at 37°C while shaking at 350 rpm for 30 minutes. Final concentrations of
850 57mM ADH d_0/d_8 (Creative Molecules) and 36mM DMTMM (Sigma-Aldrich) were added
851 to the protein samples with final concentrations of 8.3 mg/mL and 12 mg/mL respectively,
852 and incubated at 37°C with shaking at 350 rpm for 30 minutes. The reactions were
853 quenched with 100mM ammonium bicarbonate and incubated at 37°C for 30 min.
854 Samples were lyophilized and resuspended in 8M urea. Samples were reduced with
855 2.5mM TCEP incubated at 37°C for 30 min followed by alkylation with 5mM iodoacetimide
856 for 30 minutes in the dark. Samples were diluted to 1M urea using a stock of 50mM
857 ammonium bicarbonate and trypsin (Promega) was added at a 1:50 enzyme-to-substrate
858 ratio and incubated overnight at 37°C shaking at 600 rpm. 2% (v/v) formic acid was added
859 to acidify the samples following overnight digestion. All samples were run on reverse
860 phase Sep-Pak tC18 cartridges (Waters) eluted in 50% acetonitrile with 0.1% formic acid.
861 10µL of the purified peptide fractions was injected for LC-MS/MS analysis on an Eksigent
862 1D-NanoLC-Ultra HPLC system coupled to a Thermo Orbitrap Fusion Tribrid system.
863 Peptides were separated on self-packed New Objective PicoFrit columns (11cm x
864 0.075mm I.D.) containing Magic C18 material (Michrom, 3µm particle size, 200Å pore
865 size) at a flow rate of 300nL/min using the following gradient. 0-5min = 5 %B, 5-95min =
866 5-35 %B, 95-97min = 35-95 %B and 97-107min = 95 %B, where A =
867 (water/acetonitrile/formic acid, 97:3:0.1) and B = (acetonitrile/water/formic acid, 97:3:0.1).
868 The mass spectrometer was operated in data dependent mode by selecting the five most
869 abundant precursor ions (m/z 350-1600, charge state 3+ and above) from a preview scan
870 and subjecting them to collision-induced dissociation (normalized collision energy = 35%,
871 30ms activation). Fragment ions were detected at low resolution in the linear ion trap.
872 Dynamic exclusion was enabled (repeat count 1, exclusion duration 30sec).
873

874 **Solid state NMR analysis**

875 Chaperone oligomers were prepared in PBS buffer with different NaCl concentrations.
876 Lyophilized DnaJB8 uniformly labeled with ^{13}C and ^{15}N (U-^{13}C,^{15}N) was re-suspended in
877 1ml of PBS buffer in which the final NaCl concentration was 100mM or 285mM. Each
878 sample was packed into a 3.2mm MAS NMR rotor (Bruker Biospin) by sedimentation,
879 using a previously described ultracentrifugal packing tool[59] . Sedimentation was done at
880 175,000 x g force in an Optima L-100 XP Ultracentrifuge using a SW-32 Ti centrifuge
881 rotor for 1 hour. Subsequently, excess of the supernatant fluid was removed. Sample
882 tubes were washed with another 1mL buffer solution after which a second packing step
883 using same parameters was performed. Finally, supernatant was removed, spacers were
884 placed on the top of the hydrated sedimented protein oligomers, and rotors were closed
885 with the cap, sealed with a small amount of epoxy to avoid sample dehydration.
886

887 Experiments were performed on Bruker 600 MHz and 750 MHz spectrometers, at 277 K
888 temperature using triple-channel (HCN) 3.2mm MAS EFree probes. Single pulse
889 excitation (SPE) measurements were performed using a 6μs 90˚ pulse on ^{13}C, 3s recycle
890 delay, 4k scans and TPPM[60] proton decoupling of 83 kHz during acquisition.
891 1D Cross-Polarization experiments (CP) were performed using a 3.1μs 90˚ ^{1}H pulse, 2ms
892 contact time, recycle delay of 3s, 4k scans and TPPM proton decoupling of 83 kHz during
893 acquisition. Both SPE and CP experiments ran for 3.4 hours.
894 The ^{13}C-^{13}C 2D CP-DARR experiments were performed using 25ms mixing time, 0.4ms
895 contact time, 3.1μs 90° proton pulse, 6μs 90°pulse on ^{13}C, TPPM proton decoupling of
896 83 kHz, recycle delay of 2.8s, 1k scans. This experiment took 4 days and 20 hours. The
897 amino acid type and secondary structure were predicted using the PLUQ program[45]
898 based on the to chemical shifts in the 2D experiment. Linewidth calculation was done
899 using the SPARKY program[61].

900 **Simulations and synthetic NMR spectra**

901 The structure of the DnaJB8 JD in solution was determined previously using solution
902 NMR[30]. The synthetic spectrum of this domain was generated using the corresponding

903 solution NMR chemical shifts from the BMRB (entry 11417). To simulate 2D NMR spectra
904 of the other three domains MD simulations were performed on full length DnaJB8. The
905 starting DNAJB8 conformation was produced using rosetta with a fully expanded
906 conformation of the F/G and S/T domains while keeping the JD and CTD in the folded
907 conformations. MD simulations were carried out in Desmond and the simulation box was
908 prepared in Maestro[62-63]. Estimated chemical shifts of the resulting structural models were
909 generated using the SPARTA+ package[46].
910
911 **Recombinant Expression and Purification of J Domain and C-Terminal Domain**
912 Both vector constructs containing DnaJB8 JD and CTD respectively were cloned into
913 pET-29b using Gibson assembly. These vectors were transformed into *E. coli* BL-21
914 (DE3) cells and plated onto 2xLB plates with 0.05mg/mL Kanamycin. 12mL of 2xLB with
915 0.05mg/mL Kanamycin were prepared and inoculated with a single colony from each
916 plate. These small cultures were incubated overnight at 37°C while shaking at 220rpm.
917 In the morning, the 12mL culture was added to 1L of 2xLB supplemented with 0.05mg/mL
918 Kanamycin and incubated at 37°C while shaking at 220rpm. Once OD600 reached 0.6-
919 0.8 A.U., 1mL of 1M IPTG was added to induce protein expression. After incubation for
920 an additional 4 hours, the cells were harvested by spinning down the culture at 4,000g for
921 20 minutes. For preparing ^{15}N JD, a single colony was inoculated into 10mL 2xLB
922 supplemented with 0.05mg/mL Kanamycin and incubated for 7-8 hours at 37°C while
923 shaking at 220rpm. The 10mL culture was then mixed into 100mL of M9 minimal media
924 (42mM Na_2HPO_4, 22mM KH_2PO_4, 8.5mM NaCl, 0.1mM CaCl, 2mM Mg_2SO_4, 1E-4%
925 Thiamine, 0.4% Glucose, 187mM NH_4Cl, 0.05mg/mL Kanamycin) and incubated
926 overnight at 37°C while shaking at 220rpm. In the morning of the following day, the cells
927 were spun down at 2,000g for 10minutes and resuspended in 20mLs of M9 minimal media
928 containing 15N labeled NH_4Cl in place of the unlabeled molecule. This was immediately
929 added to 1L of M9 minimal media with ^{15}N labeled NH_4Cl and allowed to incubate at 37°C
930 shaking at 220rpm. Once OD600 reached 0.6-0.8 A.U., 1mL of 1M IPTG was added to
931 induce protein expression. After incubation for an additional 4 hours, the cells were

932 harvested by spinning down the culture at 4,000g for 20 minutes. The cell pellets were
933 resuspended in 20mL of soluble wash buffer (SWB) (50mM KPO_4, 300mM NaCl, 10%
934 glycerol, 1mM PMSF, 10mM BME, pH 8) and sonicated at 30% power, 5X pulse for 10
935 minutes using an Omni Sonic Ruptor 4000 (Omni International). After incubation at room
936 temperature for 1 hour, the cell lysate was spun down at 15,000g for 30 minutes to
937 separate the soluble supernatant from the insoluble pellet. The supernatant was mixed
938 with 2mL TALON® Metal Affinity Resin (Clontech) and incubated shaking at 4°C for 1
939 hour. The protein-resin slurry was loaded onto a gravity column and washed with an
940 additional 40mL of SWB. This was followed by subsequent washes: 20mL SWB with 0.5%
941 tritonX-100, 20mL SWB with adjusted 700mM NaCl, 20mL SWB with 0.1mM ATP and
942 5mM $MgCl_2$, and an additional 40mL of SWB. The protein was eluted with 16mL SWB
943 with 200mM Imidazole into 2mL fractions. After selecting for fractions with high purity, the
944 protein solution was loaded into 3.5kDa cutoff Biotech CE Dialysis Tubing (Spectrum
945 Labs) and dialyzed overnight at 4°C in 1xPBS to restore native folding. Both domain
946 constructs were further enriched by running on a GE Superdex 200 Increase 10/300
947 column in 1xPBS 1mM DTT pH 7. The protein was aliquoted and flash frozen in liquid
948 nitrogen and stored at -80°C for future use.
949
950 **Solution NMR with ^{15}N-labeled JD and CTD**
951 The ^{15}N-labeled JD was exchanged into 20mM Tris 100mM NaCl 1mM DTT pH 7 buffer
952 in preparation for solution NMR. Each HSQC run was done for 4 hours at 1 scans/min
953 with the temperature fixed at 299K. After each run, unlabeled CTD was titrated into the
954 sample at 1:1, 1:3, and 1:6 ratios sequentially. All scans were collected on an Agilent DD2
955 600MHz instrument at the UT Southwestern Biomolecular NMR Facility. Each spectrum
956 was converted into a readable format and phase corrected using NMRPipe[64]. Peak
957 assignments were based on the deposited information from BMRB (11417). The software
958 Sparky[61, 65] was used to analyze the peak shifts across all spectra.
959
960 **Circular Dichroism**

961 Recombinant $CTD_{170-232}$ domain constructs were transferred into 10mM $NaPO_4$, 150mM
962 NaF, pH 7.4 buffer at a concentration of 40µM. The experiment was run using a Jasco J-
963 815 Circular Dichroism instrument with a PMT detector using a 10 mm quartz cuvette. 6
964 accumulations were taken at a speed of 50 nm/min along the UV spectrum from 190 nm
965 to 300 nm. Spectra analysis was done using the BeStSel online software[66-67] to determine
966 secondary structural composition.
967
968 **SEC-MALS**
969 $CTD_{170-232}$ construct at a concentration of 6.6 mg/mL in 1xPBS was filtered through a 0.1
970 µm filter to remove larger impurities. The sample was further filtered using a 0.22 µm
971 centrifugal filter before 100 µL was applied to a Superdex 200 Increase 10/300 column
972 equilibrated in 1xPBS. The column was inline with a Shimadzu UV detector, a Wyatt
973 TREOS II light-scattering detector, and a Wyatt Optilab tREX differential-refractive-index
974 detector. The flow rate was 0.5 mL/min. The data were analyzed with Wyatt's ASTRA
975 software version 7.1.0.29. SEDFIT was used to calculate the dn/dc of the protein.
976
977 **CTD model generation**
978 Fragment libraries for the CTD sequence were generated using the Robetta server. 5000
979 models were produced using the *ab initio* protocol and clustered to identify unique
980 conformations. Lowest scoring models from the top clusters showed high structural
981 similarity. The identified crosslinks from the CTD in full length DnaJB8 or isolated CTD
982 were evaluated for consistency with each model in the ensemble. For acid-acid and acid-
983 lysine crosslinks a distance threshold of 21 and 16 Å, respectively, was considered as
984 satisfied and consistent with the chemistry. Distances were calculated using a custom
985 script in MATLAB ver.R2019a and the crosslink pairs were visualized using PyMOL. The
986 HYDROPRO software was used to calculate radii of hydration from structural models.
987
988
989 **Fluorescence polarization**

990 JD_{1-77} was labelled with 10x FITC-maleimide in 1xPBS 1mM TCEP for 2 hours at room
991 temperature. Excess dye was removed and the reaction quenched using a Zeba™ spin
992 desalting column. For all experiments, 0.2µM JD_{1-77} was incubated in triplicate with a
993 titration gradient of Hsp70(150µM-0µM) or $CTD_{170-232}$(150µM-0µM) in 1xPBS, 1mM
994 TCEP, pH 7.4. For competition experiments, labelled JD_{1-77} was mixed with 3.125µM CTD
995 in triplicate and incubated at room temperature for 1 hour before adding a titration gradient
996 of Hsp70(150µM-0µM). Fluorescence polarization readings were taken with excitation at
997 494nm and emission at 525nm.
998
999 **Modeling of full length DNAJB8 using Rosetta and XL-MS restraints**
1000 Given the globular conformations of the JD and CTD we considered how the crosslinks
1001 identified for the full-length protein could guide the JD-CTD interaction. Using Rosetta we
1002 assembled a monomeric conformation leveraging the JD and CTD conformations while
1003 keeping the F/G and S/T regions full expanded. This starting model was then used in a
1004 relax protocol in conjunction with crosslinks as constraints to produce an ensemble of
1005 collapsed conformations. For acid-acid and acid-lysine contacts 21 and 16 Å distance
1006 thresholds were used as restraints.
1007
1008 **Conservation mapping**
1009 DnaJB8 homolog sequences were identified using Blast[68-69] and the sequences were
1010 aligned using Clustal Omega[70]. The protein sequence alignment and structure of DnaJB8
1011 JD (PDBID 2DMX) were used as input in Al2Co[71] to map the conservation onto the
1012 structural models. The conservation was mapped onto the models in PyMOL.
1013
1014 **Coevolutionary variation analysis**
1015 The GREMLIN software[50-52] was used to identify covarying amino acid pairs from a
1016 DnaJB8 protein sequence alignment. A probability of 0.7 was used to threshold the data
1017 to identify amino acids with strong coupling.
1018

1019 **Recombinant expression and purification of HspA1A**

1020 HspA1A gene was cloned into the pMCSG7 plasmid[72] and transformed into BL-21 (DE3)
1021 cells and plated onto 2xLB plates with 0.1mg/mL ampicillin. 12mL of 2xLB with 0.1mg/mL
1022 ampicillin were prepared and inoculated with a single colony from each plate. These small
1023 cultures were incubated overnight at 37ºC while shaking at 220rpm. In the morning, the
1024 12mL culture was added to 1L of 2xLB supplemented with 0.1mg/mL ampicillin and
1025 incubated at 37°C while shaking at 220rpm. Once OD600 reached 0.6-0.8 A.U., 1mL of
1026 1M IPTG was added to induce protein expression. The cells continued to incubate
1027 overnight at 12ºC shaking at 220rpm. After incubation, the cells were lysed using a
1028 PandaPlus 2000 homogenizer (GEA) by pressing the cells with 10,000p.p.m pressure.
1029 The lysate was spun at 15,000xg for 45 minutes to remove insoluble cell components,
1030 and the resulting supernatant was mixed with 2mL TALON® Metal Affinity Resin
1031 (Clontech) and incubated at 4ºC for 1 hour. The slurry was spun down at 700xg for 2 min
1032 to remove the majority of the buffer and the beads were added onto a gravity column. The
1033 beads were washed with 6CV of wash buffer (50mM Tris, 500mM NaCl, 10mM imidazole,
1034 5mM βME, pH 8) and eluted with 5mL of elution buffer (50mM Tris, 500mM NaCl, 300mM
1035 imidazole, 5mM βME, pH 8). HspA1A containing fractions were confirmed by SDS-PAGE
1036 and pooled together for desalting. Desalting/buffer exchange was performed using a PD-
1037 10 desalting column (GE Healthcare), where HspA1A fractions were transferred into
1038 anion-exchange wash buffer (50mM Tris, 20mM NaCl, 1mM DTT, pH 8.75). The protein
1039 was loaded onto a HiTrap Q HP anion exchange column (GE Healthcare) and eluted
1040 across a gradient of anion-exchange elution buffer (50mM Tris, 1M NaCl, 1mM DTT, pH
1041 8.75). HspA1A-containing fractions were once again combined and loaded onto a
1042 Superdex™ 200 Increase 10/300 GL (GE Life Sciences) size exclusion column, where
1043 HspA1A was further purified and transferred into 1xPBS, 1mM DTT, pH 7.4 buffer for all
1044 subsequent experiments.

1045

1046 **Code availability**

1047 All DnaJB8 simulations were carried out with ROSETTA (available at
1048 https://www.rosettacommons.org/). All DNAJB8 molecular dynamics simulations were
1049 performed using Desmond (available at
1050 https://www.deshawresearch.com/resources_desmond.html). Sequence charge
1051 distributions were calculated using localCIDER (available at
1052 https://pappulab.github.io/localCIDER/).
1053

1054 **Acknowledgements**

1055 This work was supported by grants from the Welch Foundation and the Effie Marie Cain
1056 Endowed Scholarship (L.A.J.) and NIGMS R01 GM112678 (P.V.D.W.). We appreciate
1057 the help of the Structural Biology Laboratory, Biomolecular Nuclear Magnetic Resonance
1058 Facility, Electron Microscopy Core Facility, and Proteomics Core Facility at the University
1059 of Texas Southwestern Medical Center.

1060

1061 **Author Contributions**

1062 B.D.R., I.M., P.V.D.W., and L.A.J. conceived and designed the overall study. B.D.R. performed *in*
1063 *vitro* protein assays, cell models, crosslink mass spectrometry, and ROSETTA simulations. I.M.
1064 and P.V.D.W. performed ssNMR experiments and analyzed the data. S.B. performed DNAJB8
1065 CTD experiments and ROSETTA simulations. J.V.A produced mammalian cell lines and collected
1066 microscopy images. B.D.R. performed electron microscopy. B.D.R., I.M., P.V.D.W., and L.A.J.
1067 wrote the manuscript, and all authors contributed to its improvement.

1068

1069 **Competing Interests**

1070 The authors declare no competing interests.

1071
1072

1073

1074

References

1. Flaherty, K. M.; DeLuca-Flaherty, C.; McKay, D. B., Three-dimensional structure of the ATPase fragment of a 70K heat-shock cognate protein. *Nature* **1990,** *346* (6285), 623-8.
2. Wang, H.; Kurochkin, A. V.; Pang, Y.; Hu, W.; Flynn, G. C.; Zuiderweg, E. R., NMR solution structure of the 21 kDa chaperone protein DnaK substrate binding domain: a preview of chaperone-protein interaction. *Biochemistry* **1998,** *37* (22), 7929-40.
3. Bertelsen, E. B.; Chang, L.; Gestwicki, J. E.; Zuiderweg, E. R., Solution conformation of wild-type E. coli Hsp70 (DnaK) chaperone complexed with ADP and substrate. *Proc Natl Acad Sci U S A* **2009,** *106* (21), 8471-6.
4. Pellecchia, M.; Szyperski, T.; Wall, D.; Georgopoulos, C.; Wuthrich, K., NMR structure of the J-domain and the Gly/Phe-rich region of the Escherichia coli DnaJ chaperone. *J Mol Biol* **1996,** *260* (2), 236-50.
5. Szyperski, T.; Pellecchia, M.; Wall, D.; Georgopoulos, C.; Wuthrich, K., NMR structure determination of the Escherichia coli DnaJ molecular chaperone: secondary structure and backbone fold of the N-terminal region (residues 2-108) containing the highly conserved J domain. *Proc Natl Acad Sci U S A* **1994,** *91* (24), 11343-7.
6. Pellecchia, M.; Guntert, P.; Glockshuber, R.; Wuthrich, K., NMR solution structure of the periplasmic chaperone FimC. *Nat Struct Biol* **1998,** *5* (10), 885-90.
7. Choudhury, D.; Thompson, A.; Stojanoff, V.; Langermann, S.; Pinkner, J.; Hultgren, S. J.; Knight, S. D., X-ray structure of the FimC-FimH chaperone-adhesin complex from uropathogenic Escherichia coli. *Science* **1999,** *285* (5430), 1061-6.
8. Minami, Y.; Hohfeld, J.; Ohtsuka, K.; Hartl, F. U., Regulation of the heat-shock protein 70 reaction cycle by the mammalian DnaJ homolog, Hsp40. *J Biol Chem* **1996,** *271* (32), 19617-24.
9. Wall, D.; Zylicz, M.; Georgopoulos, C., The NH2-terminal 108 amino acids of the Escherichia coli DnaJ protein stimulate the ATPase activity of DnaK and are sufficient for lambda replication. *J Biol Chem* **1994,** *269* (7), 5446-51.
10. Wall, D.; Zylicz, M.; Georgopoulos, C., The conserved G/F motif of the DnaJ chaperone is necessary for the activation of the substrate binding properties of the DnaK chaperone. *J Biol Chem* **1995,** *270* (5), 2139-44.
11. Hartl, F. U., Molecular chaperones in cellular protein folding. *Nature* **1996,** *381* (6583), 571-9.
12. Cheetham, M. E.; Caplan, A. J., Structure, function and evolution of DnaJ: conservation and adaptation of chaperone function. *Cell Stress Chaperones* **1998,** *3* (1), 28-36.

1114 13. Muchowski, P. J.; Wacker, J. L., Modulation of neurodegeneration by molecular
1115 chaperones. *Nat Rev Neurosci* **2005,** *6* (1), 11-22.
1116 14. Kampinga, H. H.; Craig, E. A., The HSP70 chaperone machinery: J proteins as drivers of
1117 functional specificity. *Nat Rev Mol Cell Biol* **2010,** *11* (8), 579-92.
1118 15. Ahmad, A.; Bhattacharya, A.; McDonald, R. A.; Cordes, M.; Ellington, B.; Bertelsen, E. B.;
1119 Zuiderweg, E. R. P., Heat shock protein 70 kDa chaperone/DnaJ cochaperone complex employs
1120 an unusual dynamic interface. *Proc Natl Acad Sci U S A* **2011,** *108*, 18966-18971.
1121 16. Kityk, R.; Kopp, J.; Mayer, M. P., Molecular Mechanism of J-Domain-Triggered ATP
1122 Hydrolysis by Hsp70 Chaperones. *Mol Cell* **2018,** *69* (2), 227-237 e4.
1123 17. Rampelt, H.; Kirstein-Miles, J.; Nillegoda, N. B.; Chi, K.; Scholz, S. R.; Morimoto, R. I.;
1124 Bukau, B., Metazoan Hsp70 machines use Hsp110 to power protein disaggregation. *EMBO J*
1125 **2012,** *31* (21), 4221-35.
1126 18. Wagner, I.; Arlt, H.; van Dyck, L.; Langer, T.; Neupert, W., Molecular chaperones
1127 cooperate with PIM1 protease in the degradation of misfolded proteins in mitochondria. *EMBO*
1128 *J* **1994,** *13* (21), 5135-45.
1129 19. Nakatsukasa, K.; Huyer, G.; Michaelis, S.; Brodsky, J. L., Dissecting the ER-associated
1130 degradation of a misfolded polytopic membrane protein. *Cell* **2008,** *132* (1), 101-12.
1131 20. Jiang, Y.; Possi, P.; Kalodimos, C. G., Structural basis for client recognition and activity of
1132 Hsp40 chaperones. *Science* **2019,** *365* (6459), 1313-1319.
1133 21. Nillegoda, N. B.; Stank, A.; Malinverni, D.; Alberts, N.; Szlachcic, A.; Barducci, A.; De Los
1134 Rios, P.; Wade, R. C.; Bukau, B., Evolution of an intricate J-protein network driving protein
1135 disaggregation in eukaryotes. *Elife* **2017,** *6*.
1136 22. Hageman, J.; Rujano, M. A.; van Waarde, M. A.; Kakkar, V.; Dirks, R. P.; Govorukhina, N.;
1137 Oosterveld-Hut, H. M.; Lubsen, N. H.; Kampinga, H. H., A DNAJB chaperone subfamily with
1138 HDAC-dependent activities suppresses toxic protein aggregation. *Mol Cell* **2010,** *37* (3), 355-69.
1139 23. Karamanos, T. K.; Tugarinov, V.; Clore, G. M., Unraveling the structure and dynamics of
1140 the human DNAJB6b chaperone by NMR reveals insights into Hsp40-mediated proteostasis.
1141 *Proc Natl Acad Sci U S A* **2019**.
1142 24. Månsson, C.; Kakkar, V.; Monsellier, E.; Sourigues, Y.; Härmark, J.; Kampinga, H. H.;
1143 Melki, R.; Emanuelsson, C., DNAJB6 is a peptide-binding chaperone which can suppress amyloid
1144 fibrillation of polyglutamine peptides at substoichiometric molar ratios. *Cell Stress and*
1145 *Chaperones* **2014,** *19*, 227-239.
1146 25. Söderberg, C. A. G.; Månsson, C.; Bernfur, K.; Rutsdottir, G.; Härmark, J.; Rajan, S.; Al-
1147 Karadaghi, S.; Rasmussen, M.; Höjrup, P.; Hebert, H.; Emanuelsson, C., Structural modelling of
1148 the DnaJB6 oligomeric chaperone shows a peptide-binding cleft lined with conserved S/T-
1149 residues at the dimer interface. *Scientific Reports* **2018,** *8* (5199).
1150 26. Gillis, J.; Schipper-Krom, S.; Juenemann, K.; Gruber, A.; Coolen, S.; van den Nieuwendijk,
1151 R.; van Veen, H.; Overkleeft, H.; Goedhart, J.; Kampinga, H. H.; Reits, E. A., The DNAJB6 and
1152 DNAJB8 protein chaperones prevent intracellular aggregation of polyglutamine peptides. *J Biol*
1153 *Chem* **2013,** *288* (24), 17225-37.
1154 27. Kakkar, V.; Mansson, C.; de Mattos, E. P.; Bergink, S.; van der Zwaag, M.; van Waarde,
1155 M. A.; Kloosterhuis, N. J.; Melki, R.; van Cruchten, R. T.; Al-Karadaghi, S.; Arosio, P.; Dobson, C.
1156 M.; Knowles, T. P.; Bates, G. P.; van Deursen, J. M.; Linse, S.; van de Sluis, B.; Emanuelsson, C.;

1157 Kampinga, H. H., The S/T-Rich Motif in the DNAJB6 Chaperone Delays Polyglutamine
1158 Aggregation and the Onset of Disease in a Mouse Model. *Mol Cell* **2016**.
1159 28. Shahmoradian, S. H.; Galez-Montoya, J. G.; Schmid, M. F.; Cong, Y.; Ma, B.; Spiess, C.;
1160 Frydman, J.; Ludtke, S. J.; Chiu, W., TRiC's tricks inhibit huntingtin aggregation. *eLife* **2013,** *2*
1161 (e00710).
1162 29. Genevaux, P.; Schwager, F.; Georgopoulos, C.; Kelley, W. L., Scanning mutagenesis
1163 identifies amino acid residues essential for the in vivo activity of the Escherichia coli DnaJ
1164 (Hsp40) J-domain. *Genetics* **2002,** *162* (3), 1045-53.
1165 30. Ohnishi, S.; Tochio, N.; Koshiba, S.; Inoue, M.; Kigawa, T.; Yokoyama, S., Solution
1166 structure of the J domain of DnaJ homolog subfamily B member 8. TO BE PUBLISHED, 2006.
1167 31. D.W.A., B.; Jones, D. T., The PSIPRED Protein Analysis Workbench: 20 years on. *Nucleic*
1168 *Acids Research* **2019**.
1169 32. Jones, D. T., Protein secondary structure prediction based on position-specific scoring
1170 matrices. *J. Mol. Bio.* **1999,** *292*, 195-202.
1171 33. Kirchhofer, A.; Helma, J.; Schmidthals, K.; Frauer, C.; Cui, S.; Karcher, A.; Pellis, M.;
1172 Muyldermans, S.; Casas-Delucchi, C. S.; Cardoso, M.; Leonhardt, H.; Hopfner, K. P.; Rothbauer,
1173 U., Modulation of protein properties in living cells using nanobodies. *Nat. Struc. and Mol. Bio.*
1174 **2010,** *17* (1), 133-138.
1175 34. Kubala, M. H.; Kovtun, O.; Alexandrov, K.; Collins, B. M., Structural and thermodynamic
1176 analysis of the GFP:GFP-nanobody complex. *Protein Sci.* **2010,** *19* (12), 2389-2401.
1177 35. Trudgian, D. C.; Thomas, B.; McGowan, S. J.; Kessler, B. M.; Salek, M.; Acuto, O., CPFP: a
1178 central proteomics facilities pipeline. *Bioinformatics* **2010,** *26* (8), 1131-1132.
1179 36. Leitner, A.; Faini, M.; Stengel, F.; Aebersold, R., Crosslinking and Mass Spectometry: An
1180 Integrated Technology to Understand the Structure and Function of Molecular Machines. *Cell*
1181 *Press* **2016,** *41* (1), 20-32.
1182 37. Leitner, A.; Joachimiak, L. A.; Unverdorben, P.; Walzthoeni, T.; Frydman, J.; Förster, F.;
1183 Aebersold, R., Chemical cross-linking/mass spectometry targeting acidic residues in proteins
1184 and protein complexes. *Proc Natl Acad Sci U S A* **2014,** *111* (26), 9455-9460.
1185 38. Walzthoeni, T.; Joachimiak, L. A.; Rosenberger, G.; Röst, H. L.; Malmström, L.; Leitner, A.;
1186 Frydman, J.; Aebersold, R., xTract: software for characterizing conformational changes of
1187 protein complexes by quantitative cross-linking mass spectometry. *Nat Methods* **2015,** *12* (12),
1188 1185-1190.
1189 39. Månsson, C.; Arosio, P.; Hussein, R.; Kampinga, H. H.; Hashem, R. M.; Boelens, W. C.;
1190 Dobson, C. M.; Knowles, T. P.; Linse, S.; Emanuelsson, C., Interaction of the molecular
1191 chaperone DNAJB6 with growing amyloid-beta 42 (Abeta42) aggregates leads to sub-
1192 stoichiometric inhibition of amyloid formation. *J Biol Chem* **2014,** *289* (45), 31066-76.
1193 40. Matlahov, I.; van der Wel, P. C. A., Hidden motions and motion-induced invisibility:
1194 Dynamics-based spectral editing in solid-state NMR. *Methods* **2018,** *148*, 123-135.
1195 41. Morris, G. A.; Freeman, R., Enhancement of Nuclear Magnetic-Resonance Signals by
1196 Polarization Transfer. *J Am Chem Soc* **1979,** *101* (3), 760-762.
1197 42. Lin, H. K.; Boatz, J. C.; Krabbendam, I. E.; Kodali, R.; Hou, Z. P.; Wetzel, R.; Dolga, A. M.;
1198 Poirier, M. A.; van der Wel, P. C. A., Fibril polymorphism affects immobilized non-amyloid
1199 flanking domains of huntingtin exon1 rather than its polyglutamine core. *Nat Commun* **2017,** *8*.

1200 43. Hoop, C. L.; Lin, H. K.; Kar, K.; Magyarfalvi, G.; Lamley, J. M.; Boatz, J. C.; Mandal, A.;
1201 Lewandowski, J. R.; Wetzel, R.; van der Wel, P. C., Huntingtin exon 1 fibrils feature an
1202 interdigitated beta-hairpin-based polyglutamine core. *Proc Natl Acad Sci U S A* **2016,** *113* (6),
1203 1546-51.
1204 44. Fritzsching, K. J.; Hong, M.; Schmidt-Rohr, K., Conformationally selective
1205 multidimensional chemical shift ranges in proteins from a PACSY database purged using
1206 intrinsic quality criteria. *J Biomol NMR* **2016,** *64* (2), 115-30.
1207 45. Fritzsching, K. J.; Yang, Y.; Schmidt-Rohr, K.; Hong, M., Practical use of chemical shift
1208 databases for protein solid-state NMR: 2D chemical shift maps and amino-acid assignment with
1209 secondary-structure information. *J Biomol NMR* **2013,** *56* (2), 155-67.
1210 46. Shen, Y.; Bax, A., SPARTA+: a modest improvement in empirical NMR chemical shift
1211 prediction by means of an artificial neural network. *J Biomol NMR* **2010,** *48* (1), 13-22.
1212 47. Mandal, A.; Hoop, C. L.; DeLucia, M.; Kodali, R.; Kagan, V. E.; Ahn, J.; van der Wel, P. C.
1213 A., Structural Changes and Proapoptotic Peroxidase Activity of Cardiolipin-Bound Mitochondrial
1214 Cytochrome c. *Biophys. J.* **2015,** *109*, 1873-1884.
1215 48. Ortega, A.; Amoros, D.; Garcia, J., Prediction of hydrodynamic and other solution
1216 properties of rigid proteins from atomic and residue-level models. *Biophys. J.* **2011,** *101*, 892-
1217 898.
1218 49. Marsh, J. A.; Forman-Kay, J. D., Sequence determinants of compaction in intrinsically
1219 disordered proteins. *Biophys. J.* **2010,** *98*, 2383-2390.
1220 50. Ovchinnikov, S.; Kamisetty, H.; Baker, D., Robust and accurate prediction of residue-
1221 residue interactions across protein interfaces using evolutionary information. *Elife* **2014,** *3*.
1222 51. Kamisetty, H.; Ovchinnikov, S.; Baker, D., Assessing the utility of coevolution-based
1223 residue-residue contact predictions in a sequence- and structure-rich era. *Proc Natl Acad Sci U S*
1224 *A* **2013,** *110* (39), 15674-15679.
1225 52. Balakrishnan, S.; Kamisetty, H.; Carbonell, J. G.; Lee, S.; Langmead, C. J., Learning
1226 generative models for protein fold families. *Proteins: Structure, Function, and Bioinformatics*
1227 **2011,** *79* (4), 1061-1078.
1228 53. Mayer, M. P.; Laufen, T.; Paal, K.; McCarty, J. S.; Bukau, B., Investigation of the
1229 interaction between DnaK and DnaJ by surface plasmon resonance spectroscopy. *J Mol Biol*
1230 **1999,** *289* (4), 1131-1134.
1231 54. Holehouse, A. S.; Ahad, J.; Das, R. K.; Pappu, R. V., CIDER: Classification of Intrinsically
1232 Disordered Ensemble Regions. *Biophys. J.* **2015,** *108*, 228a.
1233 55. Jones, D. T.; Cozzetto, D., DISOPRED3: precise disordered region predictions with
1234 annotated protein-binding activity. *Bioinformatics* **2105,** *31* (6), 857-863.
1235 56. Sanders, D. W.; Kaufman, S. K.; DeVos, S. L.; Sharma, A. M.; Mirbaha, H.; Li, A.; Barker, S.
1236 J.; Foley, A.; Thorpe, J. R.; Serpell, L. C.; Miller, T. M.; Grinberg, L. T.; Seeley, W. W.; Diamond, M.
1237 I., Distinct tau prion strains propagate in cells and mice and define different tauopathies.
1238 *Neuron* **2014,** *82* (6), 1271-1288.
1239 57. Leitner, A.; Walzthoeni, T.; Aebersold, R., Lysine-specific chemical cross-linking of
1240 protein complexes and identification of cross-linking sites using LC-MS/MS and the
1241 xQuest/xProphet software pipeline. *Nat. Protocols* **2014,** *9*, 120-137.

58. Szklarczyk, D.; Gable, A. L.; Lyon, D.; Junge, A.; Wyder, S.; Huerta-Cepas, J.; Simonovic, M.; Doncheva, N. T.; Morris, J. H.; Bork, P.; Jensen, L. J.; von Mering, C., STRING v11: protein–protein association networkswith increased coverage, supporting functionaldiscovery in genome-wide experimental datasets. *Nucleic Acids Research* **2019,** *47*, D607-D613.
59. Mandal, A.; Boatz, J. C.; Wheeler, T. B.; van der Wel, P. C., On the use of ultracentrifugal devices for routine sample preparation in biomolecular magic-angle-spinning NMR. *J Biomol NMR* **2017,** *67* (3), 165-178.
60. Bennett, A. E.; Rienstra, C. M.; Auger, M.; Lakshmi, K. V.; Griffin, R. G., Heteronuclear Decoupling in Rotating Solids. *J Chem Phys* **1995,** *103* (16), 6951-6958.
61. D., G. T.; G., K. D. *SPARKY 3*, 3.110; University of California, San Francisco: San Francisco, CA, 2004.
62. *Schrödinger Release 2019-3*, D.E. Shaw Research: New York, NY, 2019.
63. Bowers, K. J.; Chow, E.; Xu, H.; Dror, R. O.; Eastwood, M. P.; Gregersen, B. A.; Klepeis, J. L.; Kolossvary, I.; Moraes, M. A.; Sacerdoti, F. D.; Salmon, J. K.; Shan, Y.; Shaw, D. E. In *Scaleable Algorithms for Molecular Dynamics Simulations on Commodity Clusters*, Proceedings of the ACM/IEEE Conference on Supercomputing (SC06), Tampa, FL, November 11-17; ACM: Tampa, FL, 2006.
64. Delaglio, F.; Grzesiek, S.; Vuister, G. W.; Zhu, G.; Pfeifer, J.; Bax, A., NMRPipe: A multidimensional spectral processing system based on UNIX pipes. *Journal of Biomolecular NMR* **1995,** *6*, 277-293.
65. Lee, W.; Tonelli, M.; Markley, J. L., NMRFAM-SPARKY: enhanced software for biomolecular NMR spectroscopy. *Bioinformatics* **2015,** *31* (8), 1325-1327.
66. Micsonai, A.; Wien, F.; Bulyáki, E.; Kun, J.; Moussong, E.; Lee, Y.; Goto, Y.; Réfrégiers, M.; Kardos, J., BeStSel: a web server for accurate protein secondary structure predicition and fold recognition from the circular dichroism spectra. *Nucleic Acids Research* **2018,** *46* (W), 315-322.
67. Micsonai, A.; Wien, F.; Kernya, L.; Lee, Y.; Goto, Y.; Réfrégiers, M.; Kardos, J., Accurate scondary structure prediction and fold recognition for circular dichroism spectroscopy. *Proc Natl Acad Sci U S A* **2015**.
68. Altschul, S. F.; Gish, W.; Miller, W.; Myers, E. W.; Lipman, D. J., Basic Local Alignment Search Tool. *J. Mol. Bio.* **1990,** *215*, 403-410.
69. Altschul, S. F.; Madden, T. L.; Schäffer, A. A.; Zhang, Z.; Miller, W.; Lipman, D. J., Gapped BLAST and PSI-BLAST: a new generation of protein database search programs. *Nucleic Acids Research* **1997,** *25*, 3389-3402.
70. Madeira, F.; Park, Y. M.; Lee, J.; Buso, N.; Gur, T.; Madhusoodanan, N.; Basutkar, P.; Tivey, A. R. N.; Potter, S. C.; Finn, R. D.; Lopez, R., The EMBL-EBI search and sequence analysis tools APIs in 2019. *Nucleic Acids Research* **2019,** *47* (W1), 636-641.
71. Pei, J.; Grishin, N. V., AL2CO: calculation of positional conservation in a protein sequence alignment. *Bioinformatics* **2001,** *17* (8), 700-712.
72. Eschenfeldt, W. H.; Lucy, S.; Millard, C. S.; Joachimiak, A.; Mark, I. D., A family of LIC vectors for high-throughput cloning and purification of proteins. *Methods Mol. Biol.* **2009,** *498*, 105-115.

Tables

Table 1. Residue distribution per domain with net charge for each domain.

Domain aa. length	Domain	Residue																				Net charge for the domain
		A	R	N	D	Q	E	G	H	I	L	K	M	F	P	S	T	Y	V	W	C	
1-75	**JD**	8	5	3	6	1	7	2	1	1	6	10	1	1	3	7	0	5	4	2	1	+2
76-148	**F/G**	6	5	2	5	0	5	13	2	1	2	0	1	14	6	6	3	2	0	1	0	-5
149-185	**S/T**	0	0	1	0	0	1	7	1	0	1	1	3	4	0	15	4	0	1	0	1	0
186-232	**CTD**	0	2	3	2	3	6	4	7	2	2	6	1	0	0	2	3	0	6	1	0	0

1306 **Figure Legends**

1307

1308 **Figure 1. Electrostatic interactions drive chaperone and co-chaperone interactions. (A)**
1309 Structural superposition of a HspA1A structural model (blue) with a crystal structure of DnaK-
1310 DnaJ (green and cyan, respectively; PDBID: 5NRO) shows good agreement. **(B-C)** Electrostatic
1311 surface potential of DnaJB8 JD docked into the JD binding site on HspA1A is shown in cartoon
1312 representation and is colored in black. Binding mode is based on the DnaJ-DnaK coordinates.
1313 Basic surface on helix 2 docks onto the HspA1A surface. Electrostatic surface potential of
1314 HspA1A with docked DnaJB8 JD is shown in cartoon representation and is colored in black. The
1315 HspA1A surface presents an acidic face that complements the basic DnaJB8 JD surface. Highly
1316 acidic potential is shown in red and highly basic is shown in blue. **(D)** Cartoon schematic of
1317 DnaJB8 colored according to domain annotation: JD (red), F/G rich(blue), S/T rich (cyan), and
1318 CTD (green). **(E)** PSIPRED secondary structure analysis of the DnaJB8 sequence. Probabilities
1319 for helix, sheet, and random coil assignments are colored pink, yellow and blue, respectively. **(F)**
1320 Charge-based analysis of the DnaJB8 sequence. Sequence charge distribution of DnaJB8 is
1321 shown using Net Protein Charge per Residue (NPCR). Basic regions are shown in blue and acidic
1322 regions are shown in red. Basic face of helix 2 is highlighted along with the corresponding acidic
1323 face of the CTD. The helices for JD are shown as grey rectangles. **(G)** DISOPRED analysis of
1324 the DnaJB8 sequence. Regions above the red-dashed line are predicted to be disordered.

1325

1326 **Figure 2. DnaJB8 forms oligomers in cells.** (**A**) Cartoon schematics for the DnaJB-Clover and
1327 Clover constructs used in the mammalian experiments. DnaJB8 is colored as in Figure 1. Clover
1328 is colored in green. (**B**) Representative images of cells expressing DnaJB8-Clover and Clover.
1329 Clover and DAPI fluorescence signal are shown in green and blue, respectively. 5um scale bar is
1330 shown in white. (**C**) Quantification of DnaJB8-Clover and Clover puncta in high and low protein
1331 level expressing cell lines. In each analysis at least 2000 cells were counted. (**D**) Western blot
1332 analysis of DnaJB8-Clover and Clover proteins isolated from mammalian cell lines. Total (T),
1333 elutions (E) and crosslinked elutions (XL) of each condition are shown. Western blot was probed
1334 with GFP antibodies. (**E**) XL-MS contact map of DnaJB8-Clover crosslinks (orange boxes)
1335 identified using DMTMM and ADH. The axes are colored in red and green for JD and CTD,
1336 respectively. Crosslink pairs between JD-CTD, JD-JD and CTD-CTD are shown in dashed boxes
1337 colored grey, red and green, respectively.

1338

1339 **Figure 3. DnaJB8 forms oligomers *in vitro*. (A)** DLS time-course of DnaJB8. Average radius of
1340 hydration (R_h) of triplicate samples starts at ~15nm and increases over time to ~90nm. An arrow
1341 indicates the time point where DnaJB8 was observed under TEM. **(B)** TEM image of DnaJB8
1342 oligomers. 200nm scale bar is shown in black. Length of oligomeric assemblies is ~90nm with a
1343 ~20nm width. **(C)** XL-MS contact map of DnaJB8 crosslinks identified using DMTMM and ADH
1344 (black) and DSS (grey). The axes are colored in red and green for JD and CTD, respectively.
1345 Crosslink pairs between JD-CTD, JD-JD and CTD-CTD are shown in dashed boxes colored grey,
1346 red and green, respectively. **(D)** DLS time-course of DnaJB8 under elevated ionic strength
1347 conditions (285mM NaCl). Average R_h of triplicate samples is ~13.7±1.2 nm. **(E)** TEM image of
1348 DnaJB8 oligomers. 50nm scale bar is shown in black. The oligomers appear as spherical masses
1349 with an average diameter of ~15nm. **(F)** Contact map of DnaJB8 crosslinks identified using
1350 ADH/DMTMM in the presence of high ionic strength. The axes are colored in red and green for
1351 JD and CTD, respectively. JD-JD and CTD-CTD crosslinks are shown in dashed boxes colored
1352 in red and green, respectively.

1353

1354 **Figure 4. Solid-state NMR of DnaJB8 oligomers at physiological and high ionic strength.**

(A) 2D ^{13}C-^{13}C ssNMR spectrum of U-^{13}C,^{15}N-labeled DnaJB8 oligomers in PBS, using 25 ms DARR mixing. **(B)** Corresponding 2D ssNMR spectrum at elevated ionic strength (285mM NaCl). **(C-D)** Boxed Ala and Ser regions from panel "A". The experimental peak pattern (black) is well resolved and is similar to the expected pattern of the folded JD in solution (red; middle). Green spectra (right) represent simulated signals predicted for Ala and Ser in our models of the non-JD domains, shown with enhanced broadening reflecting the heterogeneity seen in the experiments. 1D spectra on far left show slices through the experimental 2D data, along with selected peak widths (in kHz). **(E)** ^{13}C 1D spectra at physiological (top) and elevated ionic strength (bottom) that show rigid residues (black, CP), rigid and mobile residues (green, SPE) and only mobile residues (red, INEPT). See also text. **(F)** Electrostatic surface potential of the DnaJB8 JD. Strongly positive area surrounding helix 2 is highlighted by the grey ellipse. Highly positive and negative potentials are colored blue and red, respectively. White color represents neutral charge. **(G)** The same view showing the location of Ala with narrow peaks at physiological salt levels (panel "A") which disappear at high ionic strength (panel "B"). **(H,I)** Same model after 90° y-rotation showing two additional smaller positively charged regions and the nearby location of Alanines that disappear at high ionic strength.

Figure 5. Isolated JD and CTD proteins are monomeric. (A) Cartoon schematic for the full length DnaJB8 and the two domain fragments: JD_{1-77} and $CTD_{170-232}$. Domains are colored as in Figure 1. **(B)** SEC chromatograms of JD_{1-77}(red), $CTD_{170-232}$(green) and LMW standards (blue). JD_{1-77} and $CTD_{170-232}$ elute at apparent molecular weights of 14kDa and 6.5kDa, respectively. **(C)** SDS-PAGE coomassie gel of crosslinked JD_{1-77} and $CTD_{170-232}$ crosslinked with either DMTMM only or additionally with ADH. **(D)** Contact map of ADH/DMTMM crosslinks identified for JD_{1-77}(red), $CTD_{170-232}$(green) and full length DnaJB8 (black). The axes are colored in red and green for JD and CTD, respectively. Crosslink pairs between JD-JD and CTD-CTD are shown in dashed boxes colored in red and green, respectively. **(E)** Rosetta *ab initio* models of CTD. The structural models are consistent with R_h values derived from DLS (dashed line). Structural overlay of low energy scoring models reveals consistent pleated β-sheet fold. Models are shown in cartoon representation and are colored in green. **(F)** Histogram of the number of intra-domain crosslinks that are consistent with crosslink chemistry geometry ("satisfied") in the ensemble of 5000 models. One model satisfies 13 out of 14 possible crosslinks identified in our experiments. Crosslinks are mapped onto best matching CTD structural model. CTD is shown in cartoon representation and is colored in white. Sites of crosslink are shown as spheres and are colored red or blue for D/E and K, respectively. Dashed yellow lines connect linked amino acid pairs.

Figure 6. JD and CTD interact through charge complementary surfaces.
(A) Schematic of the JD_{1-77} and $CTD_{170-232}$ constructs used in fluorescence polarization and XL-MS binding experiments. **(B)** Fluorescence polarization (FP) titration measuring interaction between JD_{1-77}-FITC and a concentration range of unlabeled $CTD_{170-232}$. FP experiments were performed in triplicate and shown as averages with standard deviation. Non-linear regression fit of the binding curve reveals a $K_{d,app}$ of 0.575μM for this interaction. **(C)** Contact map of ADH/DMTMM crosslinks identified from an incubated JD_{1-77} and $CTD_{170-232}$ sample (grey) and full length DnaJB8 (black). The axes are colored in red and green for JD and CTD, respectively. Helix 2 and 3 are shown in grey on the x-axis. Crosslink pairs between JD-CTD are shown in a dashed box colored in grey. **(D)** Schematic for the chemical shift experiment with U-^{15}N JD and titrated with unlabeled CTD. Domains are colored as in Figure 1. HSQC solution NMR spectrum of ^{15}N-labelled JD_{1-77} against a titration of $CTD_{170-232}$: 0x (yellow), 1x (red), 3x (purple), 6x (blue). DnaJB8 JD peak assignments were transferred from deposited data (BMRB:11417). **(E)** Insets of peaks with highest observed chemical shifts: H31, L28, L26, R29. Peaks were colored as in **D**. **(F)** Histogram of chemical shifts by residue from 1-77. Average chemical shift value of ~0.019ppm is

1405 denoted by the red line (excludes prolines). **(G)** DnaJB8 JD structure illustrating the location of
1406 helix 2 (pdbid:2DMX). Structure is shown in cartoon representation and colored in white. **(H)**
1407 Mapping chemical shifts onto the DnaJB8 JD structure. JD is shown in surface representation
1408 and is colored according to chemical shifts from low (0.0 ppm) colored in yellow to high colored
1409 in red (0.04 ppm). **(I)** Electrostatic potential mapping onto DnaJB8 JD structure. JD is shown in
1410 surface representation and colored according to electrostatic. Highly acidic potential is shown in
1411 red and highly basic is shown in blue.
1412
1413 **Figure 7. Sequence and structural properties of the JD-CTD interaction.** (**A**) XL-MS-based
1414 refinement of full length expanded DnaJB8 monomer. Cartoon representation of DnaJB is shown
1415 in fully expanded conformation and collapsed conformation, colored by domain as in Figure 1.
1416 Aromatic amino acids in the F/G and S/T domains are shown as spheres and colored according
1417 to the domain. Residues in Helix 5 (H5) are shown as spheres and colored in magenta. (**B**)
1418 Charge complementary surfaces on the JD and CTD in the full-length DnaJB8 model mediate the
1419 interaction. Highly acidic potential is shown in red (- sign) and highly basic is shown in blue (+
1420 sign) and colored by conservation. **(C)** GREMLIN sequence-based covariance analysis identified
1421 high confidence covarying amino acids on DnaJB8 that localize within the JD (red sector), within
1422 CTD (green sector) and across JD-CTD (grey sector). XL-MS identified for full length DnaJB8
1423 (black) overlap with the covarying regions. Covarying positions localizing to amino acids in F/G
1424 domain are shown in brown and co-localize with crosslinks to this surface (black). **(D)** Three amino
1425 acids: D37, E43, and S50 are shown to covary with the CTD (red spheres).
1426
1427 **Figure 8. CTD and HSPA1A compete for the same basic binding surface on DnaJB8 JD. (A-**
1428 **B)** Acidic surfaces on HspA1A and CTD interact with basic surface on DnaJB8 JD. In the fully
1429 extended DnaJB8 conformation, the CTD (green) is not engaged with the DnaJB8 JD (red) and
1430 is accessible to HspA1A binding. In the collapsed DnaJB8 conformation, the CTD (green) is with
1431 the engaged DnaJB8 JD and not accessible to HspA1A binding. DnaJB8 is shown in cartoon and
1432 is colored according to domains as in Figure 1. HspA1A is shown in cartoon representation and
1433 is colored in blue. **(C)** Experimental workflow of experiments to determine competition between
1434 Hsp70 and CTD for JD binding. **(D)** Normalized FP binding curves measuring affinity between JD-
1435 CTD (green) and JD-Hsp70 (grey). Preincubation of JD-CTD followed by addition of Hsp70
1436 (purple) shows delay in binding consistent with a competitive binding model. FP experiments were
1437 performed in triplicate and shown as averages with standard deviation. Fit was performed using
1438 non-linear regression analysis in GraphPad Prism. **(E)** JD-HspA1A crosslinks mapped onto JD-
1439 Hsp70 model. JD and HspA1A are shown in cartoon representation and colored white and black
1440 respectively. Sites of crosslink are shown as spheres and are colored red or blue for
1441 aspartic/glutamic and lysines, respectively. Dashed yellow lines connect linked amino acid pairs.
1442 **(F)** Schematic of proposed DnaJB8 model. Individual domains are shown as JD (red spheres),
1443 CTD (green spheres), F/G+S/T (light blue spheres), and both Hsp70 (dark blue spheres) and
1444 substrate (purple line) are shown. DnaJB8 domains are displayed relative to the R_h values derived
1445 from DLS experiments (Hsp70 not drawn to scale). DnaJB8 forms a fundamental oligomeric
1446 species through aromatic contacts in the F/G and S/T domains ranging from monomer to octamer.
1447 In the JD:CTD engaged state, these structures grow over time to form larger polydisperse
1448 oligomers(>100nm). The JD:CTD disengaged state (bottom) demonstrates our hypothesis where
1449 substrate bound to a uniform minimal unit of DnaJB8 disrupts the JD:CTD interaction. This leads
1450 to the recruitment of Hsp70 along the JD-CTD binding face, and the handoff of substrate to Hsp70.
1451

1452

Figure 1

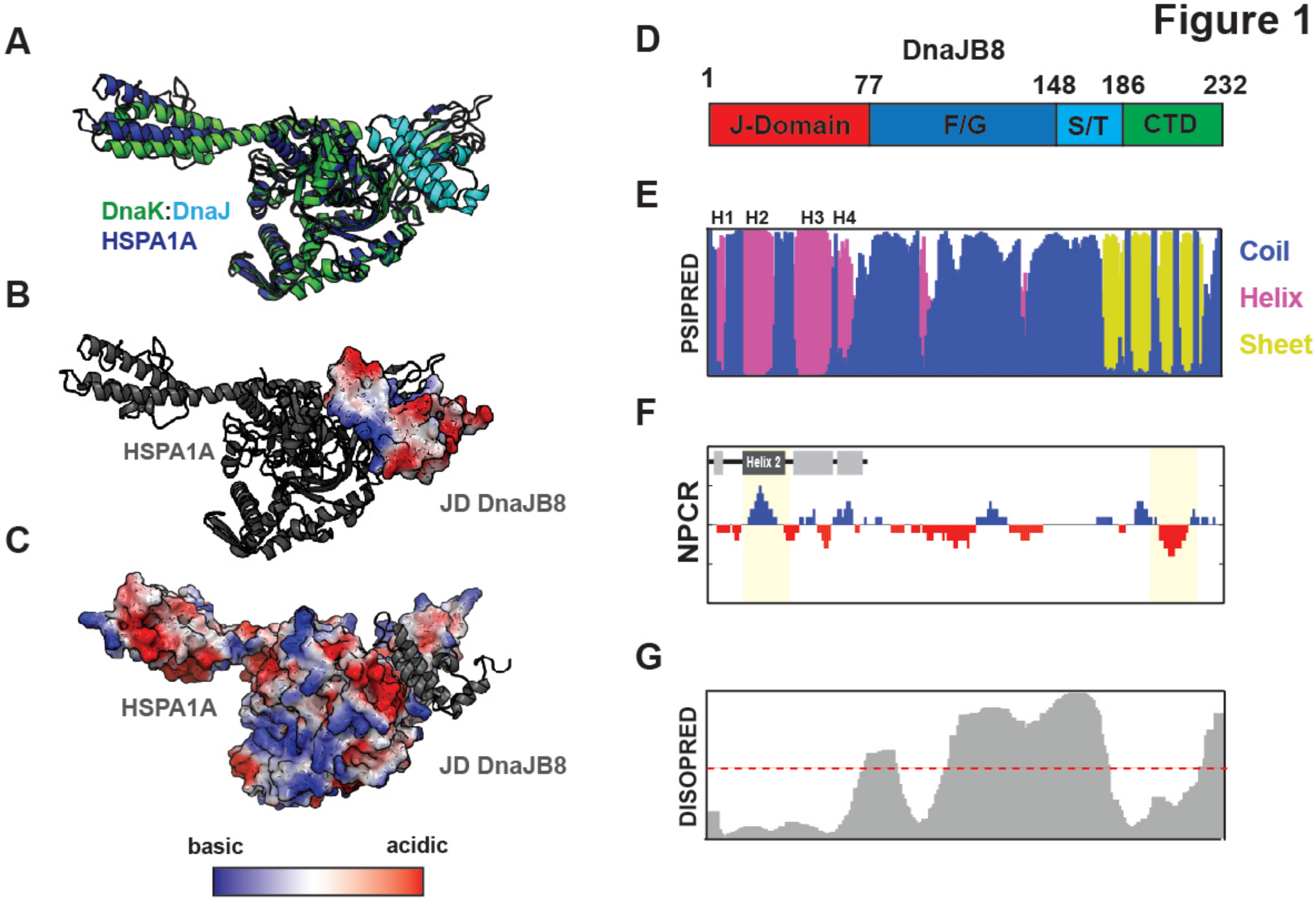
A
DnaK:DnaJ
HSPA1A
B
HSPA1A
JD DnaJB8
C
HSPA1A
JD DnaJB8
basic
acidic
D
DnaJB8
1
77
148
186
232
J-Domain
F/G
S/T
CTD
E
H1 H2 H3 H4
PSIPRED
Coil
Helix
Sheet
F
Helix 2
NPCR
G
DISOPRED

Figure 2

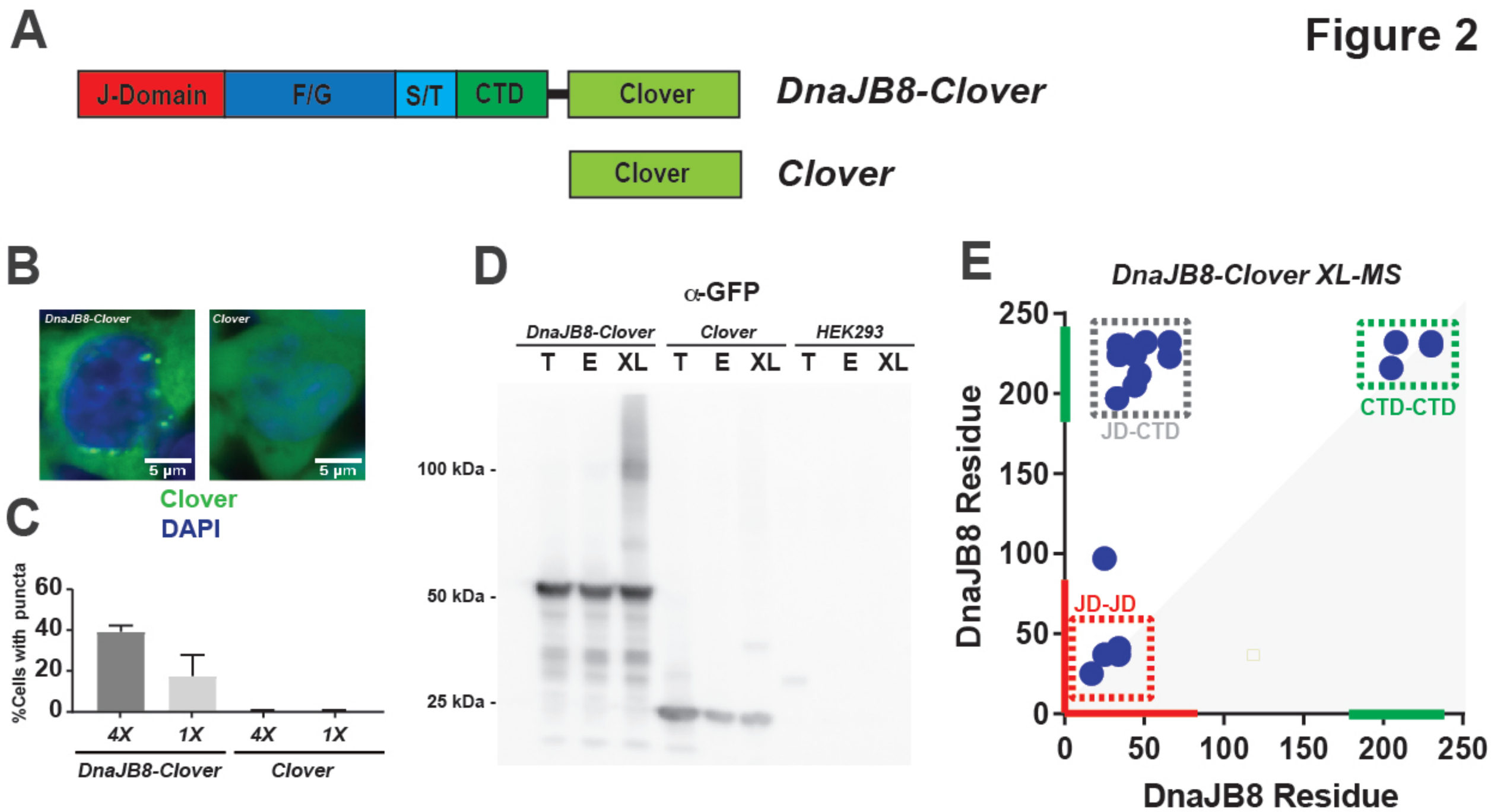
A
J-Domain
F/G
S/T
CTD
Clover
DnaJB8-Clover
Clover
Clover
B
DnaJB8-Clover
Clover
5 µm
5 µm
Clover
DAPI
C
%Cells with puncta
60
40
20
0
4X
1X
4X
1X
DnaJB8-Clover
Clover
D
α-GFP
DnaJB8-Clover
Clover
HEK293
T E XL T E XL T E XL
100 kDa -
50 kDa -
25 kDa -
E
DnaJB8-Clover XL-MS
DnaJB8 Residue
250
200
150
100
50
0
JD-CTD
CTD-CTD
JD-JD
0 50 100 150 200 250
DnaJB8 Residue

Figure 3

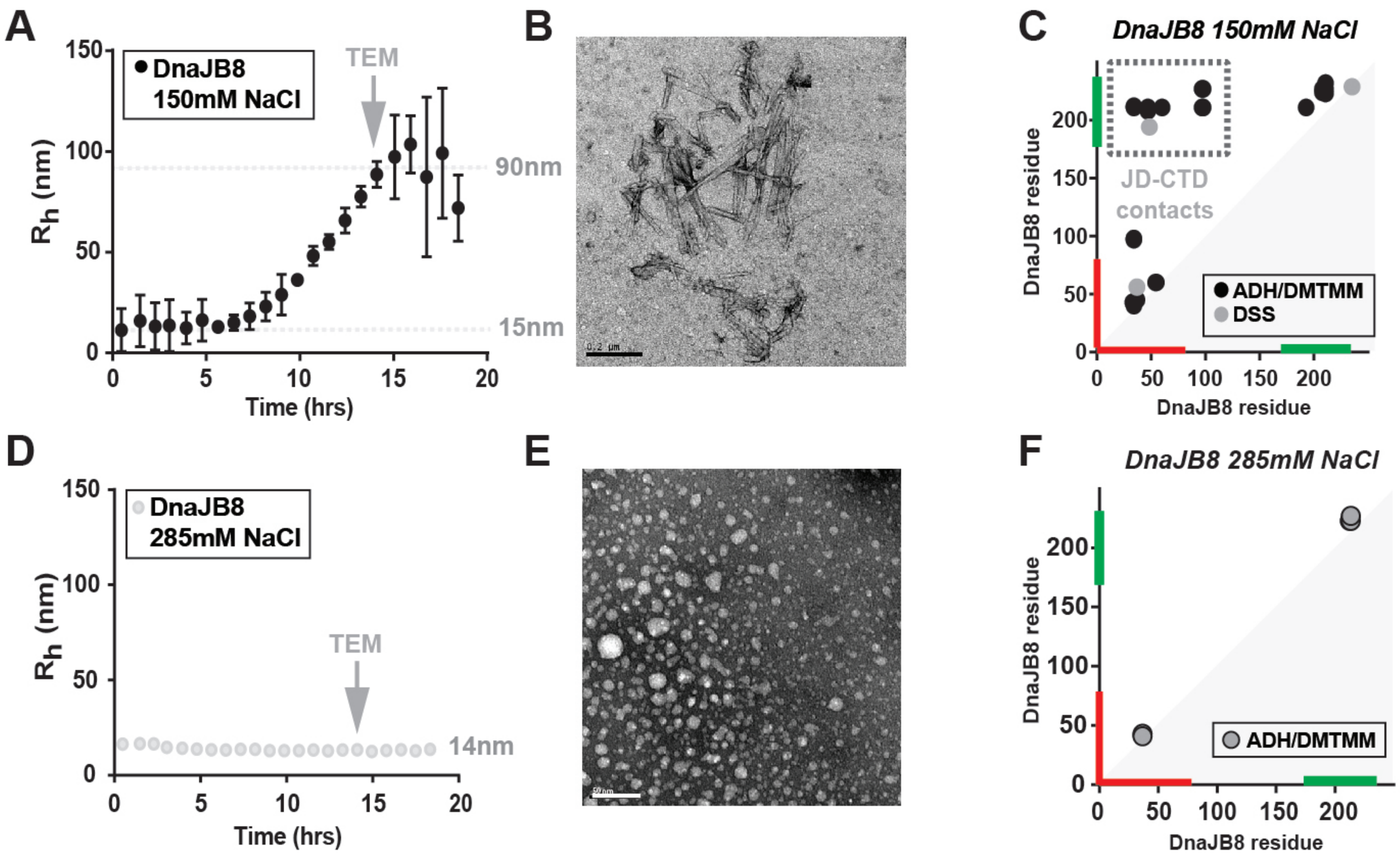
A
DnaJB8
150mM NaCl
TEM
90nm
15nm
R_h (nm)
Time (hrs)
B
C
DnaJB8 150mM NaCl
JD-CTD
contacts
ADH/DMTMM
DSS
DnaJB8 residue
DnaJB8 residue
D
DnaJB8
285mM NaCl
TEM
14nm
R_h (nm)
Time (hrs)
E
F
DnaJB8 285mM NaCl
ADH/DMTMM
DnaJB8 residue
DnaJB8 residue

Figure 4

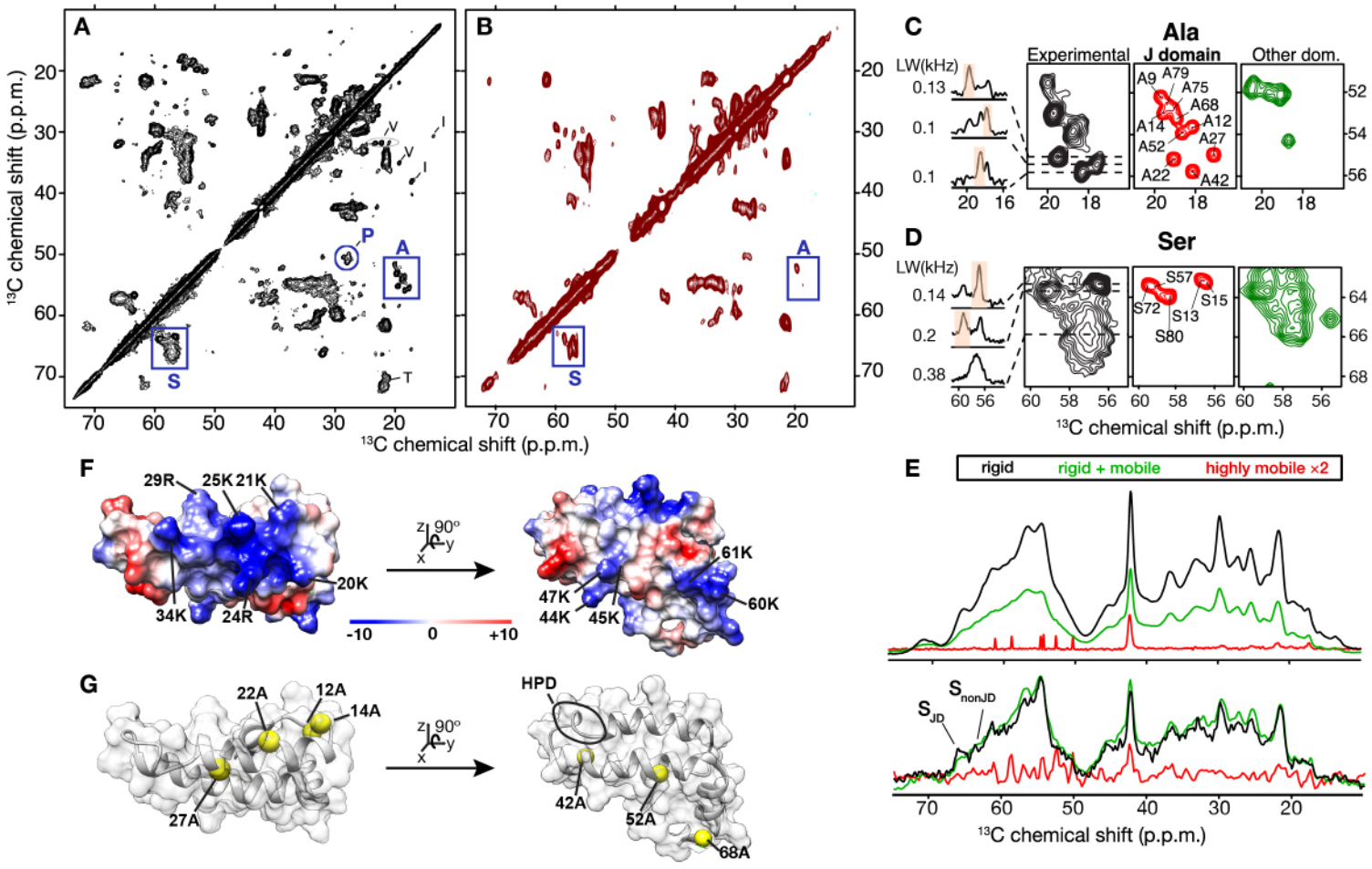
A
B
C
D
E
F
G
^{13}C chemical shift (p.p.m.)
P
A
S
V
I
T
Ala
Experimental
J domain
Other dom.
LW(kHz)
A9
A79
A75
A68
A14
A12
A52
A27
A22
A42
Ser
S57
S72
S15
S13
S80
rigid
rigid + mobile
highly mobile ×2
S_{JD}
S_{nonJD}
29R
25K
21K
20K
34K
24R
61K
47K
44K
45K
60K
-10
0
+10
22A
12A
14A
27A
HPD
42A
52A
68A
90°

Figure 5

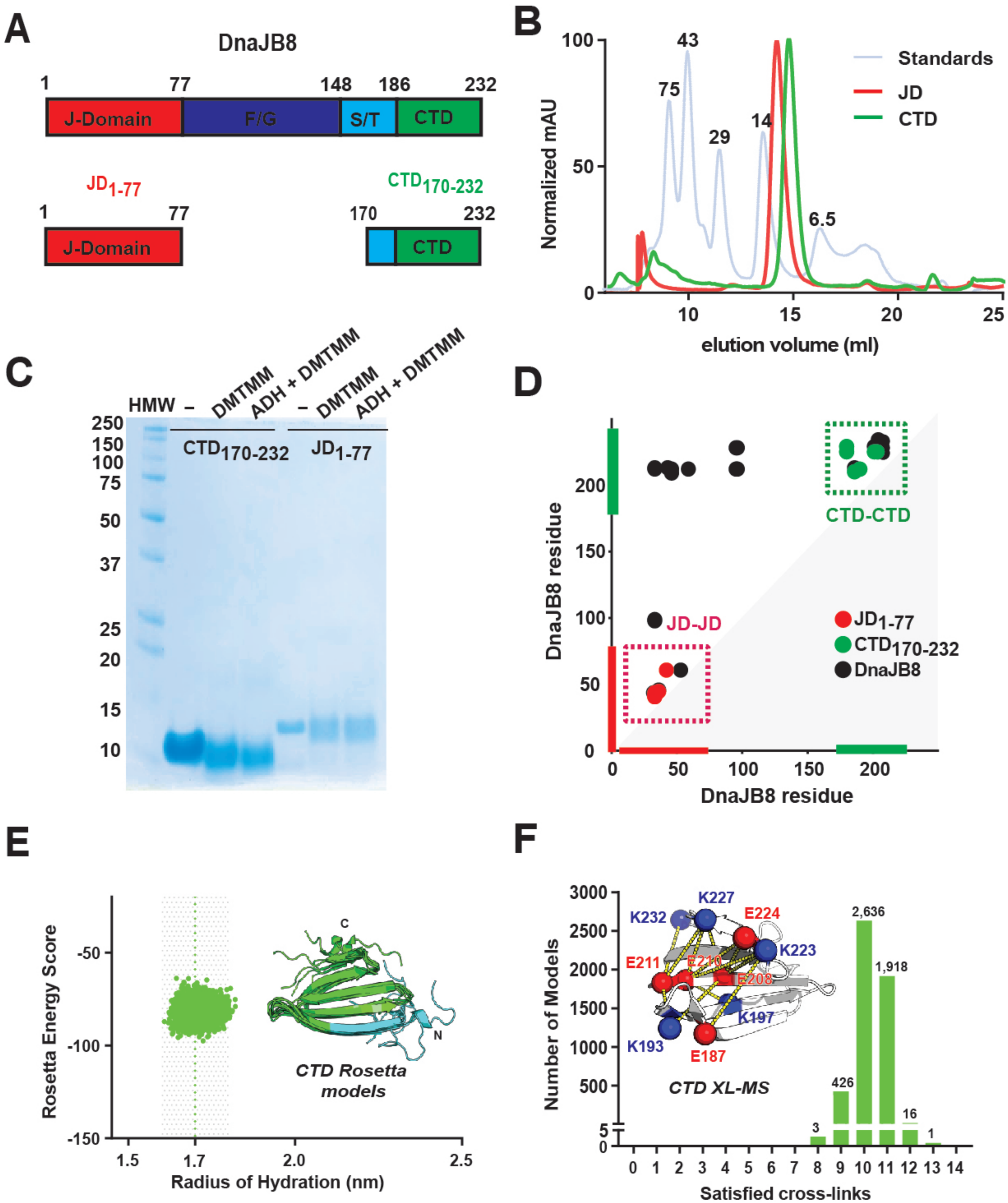
A
DnaJB8
1
77
148
186
232
J-Domain
F/G
S/T
CTD
JD1-77
CTD170-232
J-Domain
CTD
B
Standards
JD
CTD
Normalized mAU
elution volume (ml)
43
75
29
14
6.5
C
HMW
–
DMTMM
ADH + DMTMM
CTD170-232
JD1-77
250
150
100
75
50
37
25
20
15
10
D
DnaJB8 residue
CTD-CTD
JD-JD
JD1-77
CTD170-232
DnaJB8
E
Rosetta Energy Score
Radius of Hydration (nm)
CTD Rosetta models
C
N
F
Number of Models
Satisfied cross-links
K227
K232
E224
K223
E211
E210
E208
K197
K193
E187
CTD XL-MS
2,636
1,918
426
3
16
1

Figure 6

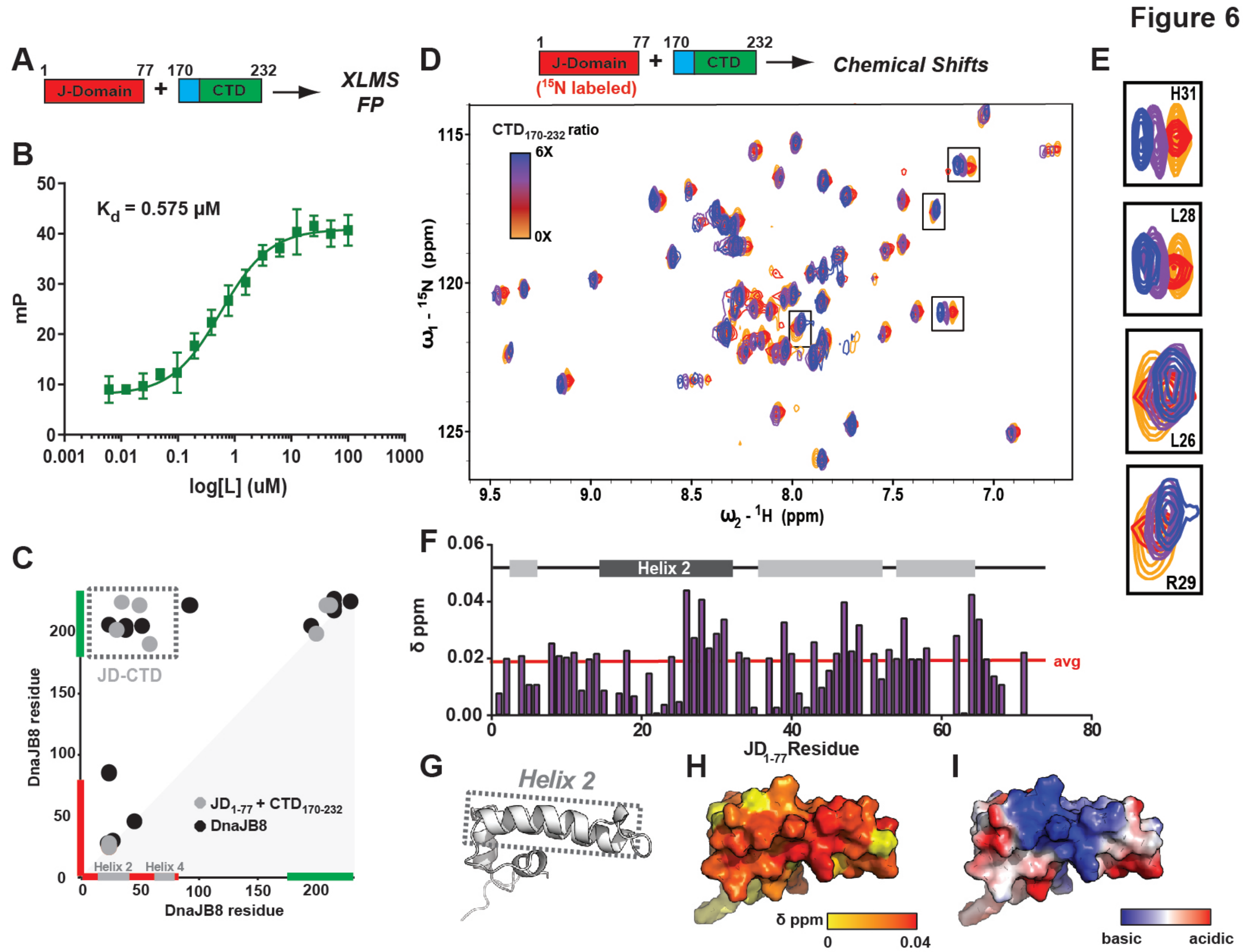
A
1
77
170
232
J-Domain
CTD
XLMS
FP
B
K_d = 0.575 μM
mP
log[L] (uM)
C
JD-CTD
DnaJB8 residue
JD_{1-77} + $CTD_{170-232}$
DnaJB8
Helix 2
Helix 4
D
(^{15}N labeled)
Chemical Shifts
$CTD_{170-232}$ ratio
6X
0X
ω_1 - ^{15}N (ppm)
ω_2 - ^{1}H (ppm)
E
H31
L28
L26
R29
F
Helix 2
δ ppm
avg
JD_{1-77} Residue
G
Helix 2
H
δ ppm
I
basic
acidic

Figure 7

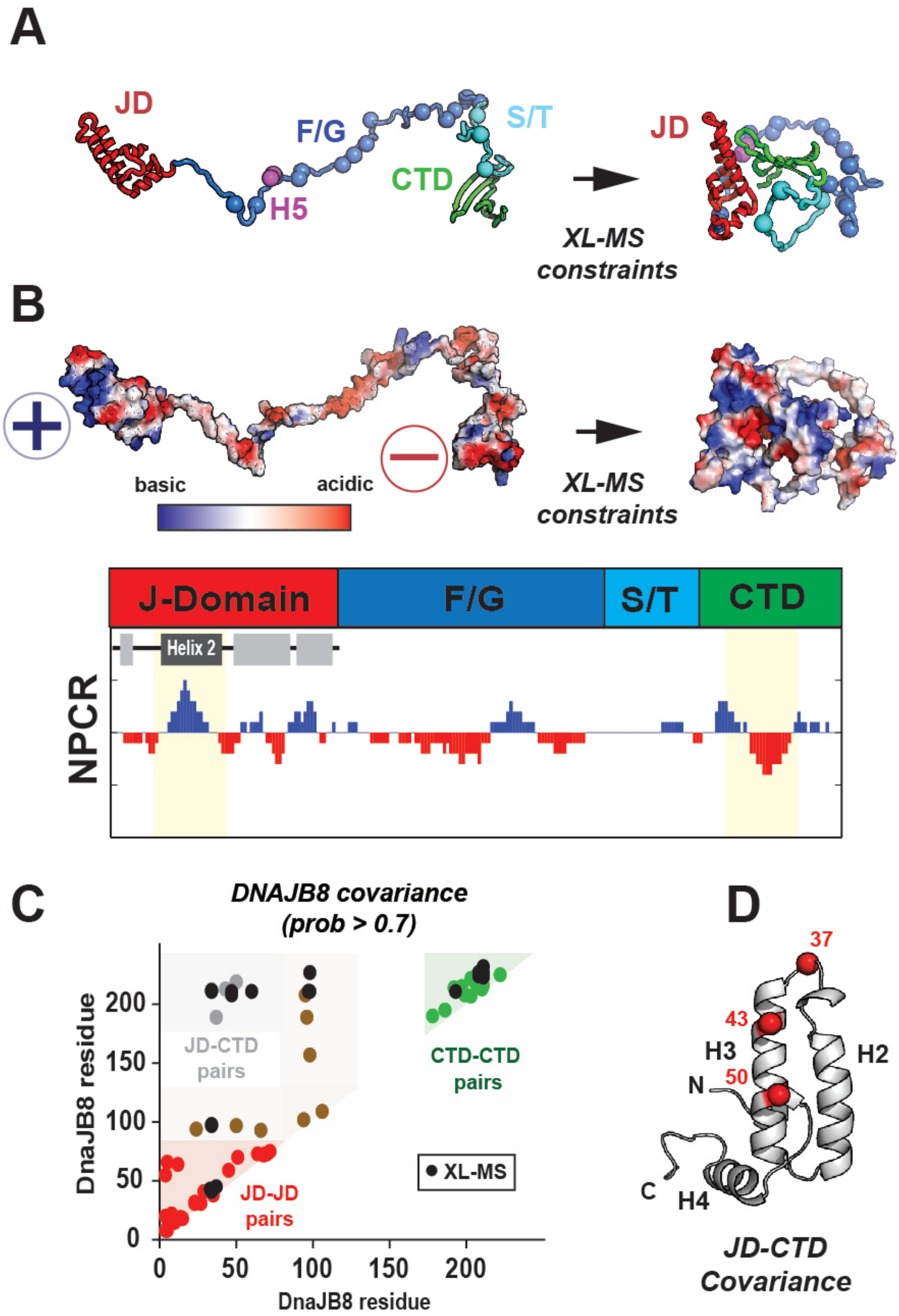
A
JD
F/G
S/T
CTD
H5
JD
XL-MS
constraints
B
basic
acidic
XL-MS
constraints
J-Domain
F/G
S/T
CTD
Helix 2
NPCR
C
DNAJB8 covariance
(prob > 0.7)
DnaJB8 residue
JD-CTD
pairs
CTD-CTD
pairs
XL-MS
JD-JD
pairs
0
50
100
150
200
DnaJB8 residue
D
37
43
H3
H2
N
50
C
H4
JD-CTD
Covariance

Figure 8

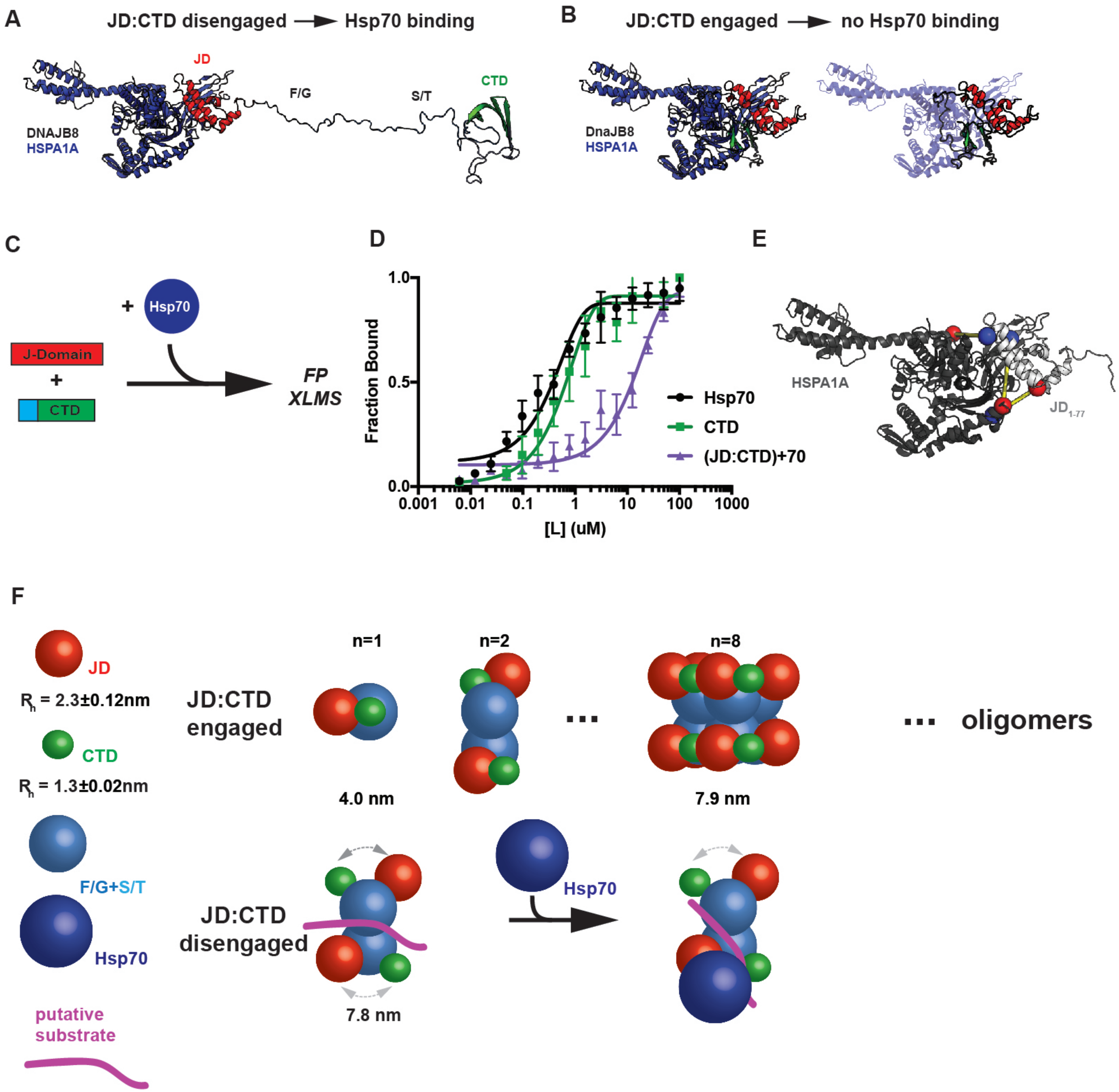
A
JD:CTD disengaged → Hsp70 binding
JD
F/G
S/T
CTD
DNAJB8
HSPA1A
B
JD:CTD engaged → no Hsp70 binding
DnaJB8
HSPA1A
C
Hsp70
J-Domain
CTD
FP
XLMS
D
Fraction Bound
1.0
0.5
0.0
0.001
0.01
0.1
1
10
100
1000
[L] (uM)
Hsp70
CTD
(JD:CTD)+70
E
HSPA1A
JD1-77
F
JD
Rh = 2.3±0.12nm
CTD
Rh = 1.3±0.02nm
F/G+S/T
Hsp70
putative
substrate
JD:CTD
engaged
n=1
n=2
n=8
4.0 nm
7.9 nm
... oligomers
JD:CTD
disengaged
7.8 nm
Hsp70